The Gravity Field, Orientation, and Ephemeris of Mercury from MESSENGER Observations after Three Years in Orbit

Erwan Mazarico,[1,2] Antonio Genova,[1,2] Sander Goossens,[3,2] Frank G. Lemoine,[2] Gregory A. Neumann,[2] Maria T. Zuber,[1] David E. Smith,[1] and Sean C. Solomon[4,5]

Correspondence to: E. Mazarico, erwan.m.mazarico@nasa.gov

[1]Department of Earth, Atmospheric and Planetary Sciences, Massachusetts Institute of Technology, Cambridge, Massachusetts, USA.

[2]NASA Goddard Space Flight Center, Greenbelt, Maryland, USA.

[3]Center for Research and Exploration in Space Science and Technology, University of Maryland, Baltimore County, Baltimore, Maryland, USA.

This article has been accepted for publication and undergone full peer review but has not been through the copyediting, typesetting, pagination and proofreading process, which may lead to differences between this version and the Version of Record. Please cite this article as doi: 10.1002/2014JE004675

Abstract.

We have analyzed three years of radio tracking data from the MESSENGER spacecraft in orbit around Mercury and determined the gravity field, planetary orientation, and ephemeris of the innermost planet. With improvements in spatial coverage, force modeling, and data weighting, we refined an earlier global gravity field both in quality and resolution, and we present here a spherical harmonic solution to degree and order 50. In this field, termed HgM005, uncertainties in low-degree coefficients are reduced by an order of magnitude relative to the earlier global field, and we obtained a preliminary value of the tidal Love number k_2 of 0.451±0.014. We also estimated Mercury's pole position, and we obtained an obliquity value of 2.06 ± 0.16 arcmin, in good agreement with analysis of Earth-based radar observations. From our updated rotation period (58.646146 $\pm$ 0.000011 days) and Mercury ephemeris, we verified experimentally the planet's 3:2 spin-orbit resonance to greater accuracy than previously possible. We present a detailed

[4]Lamont-Doherty Earth Observatory,
Columbia University, Palisades, New York,
USA.

[5]Department of Terrestrial Magnetism,
Carnegie Institution of Washington,
Washington, District of Columbia, USA.

analysis of the HgM005 covariance matrix, and we describe some near-circular frozen orbits around Mercury that could be advantageous for future exploration.

1. Introduction

The gravity field of a planet provides fundamental information on the structure and evolution of the planet's interior. In this paper, we report a new solution for the gravity field of Mercury, here termed HgM005, developed at the NASA Goddard Space Flight Center (GSFC) from nearly three years of radiometric tracking data from the MErcury Surface, Space ENvironment, GEochemistry, and Ranging (MESSENGER) spacecraft. The analysis presented here includes orbital observations between March 2011 and February 2014 spanning more than six Mercury years, or about 20 Mercury spin periods, as well as data from the three Mercury flybys in 2008 and 2009. In comparison to the previous MESSENGER models of Mercury's gravity field [*Smith et al.*, 2012; *Genova et al.*, 2013], HgM005 is of higher resolution, to spherical harmonic degree and order 50, and includes refined force modeling that improves confidence in the solution.

1.1. History

Mercury, the innermost planet of the solar system, has been observed by humans since earliest time. Its proximity to the Sun made it challenging to study, and the planet remained largely a mystery even as our knowledge of other celestial bodies increased through ground-based observations and early spacecraft exploration. Mercury's orbit around the Sun was characterized early, and the precession of its perihelion provided Einstein with an early experimental confirmation of general relativity, but the rotation period of Mercury was not reliably measured until 1965. Indeed, Mercury was earlier thought to be in a synchronous spin-orbit resonance, with a rotation period equal to its orbital period of $\sim$ 88 days. *Pettengill and Dyce* [1965] reported a much shorter

rotation period, 59 ± 5 days, from ground-based radar measurements. Additional radar observations, and surface images by NASA's Mariner 10 spacecraft [*Klaasen*, 1976] further confirmed that Mercury is in a 3: 2 resonance.

The two equatorial flybys and one high-inclination flyby by Mariner 10 in 1974 and 1975 also provided the first measurements of Mercury's gravity field. *Anderson et al.* [1987] estimated the gravitational parameter [$GM = (2.203209 \pm 0.000091) \times 10^{13}$ m^3 s^{-2}, where M is Mercury's mass and G is the gravitational constant] and quadrupole field [represented by the two second-degree terms in the spherical harmonic expansion of the gravitational potential, $\bar{C}_{20} = (-2.68 \pm 0.9) \times 10^{-5}$ and $\bar{C}_{22} = (1.58 \pm 0.8) \times 10^{-5}$, 4π-normalized]. Unfortunately, the historical radio tracking data from the Mariner 10 flybys are no longer available because of a non-standard format and missing documentation.

The MESSENGER spacecraft made three equatorial flybys of Mercury at an altitude of closest approach of $\sim$ 200 km in 2008 and 2009. As reported by *Smith et al.* [2010], this geometry enabled good recovery of the difference in the equatorial moments of inertia [$\bar{C}_{22} = (1.26 \pm 0.12) \times 10^{-5}$]. In contrast, the geometry was not favorable to the recovery of the gravitational polar flattening ($\bar{C}_{20}$), and *Smith et al.* [2010] cautioned that the estimated value of $(-0.86 \pm 0.30) \times 10^{-5}$ for that quantity was implausible given its implications for interior models.

With ground-based radar observations obtained during 2002–2006, *Margot et al.* [2007] measured precisely the spin-axis orientation and the amplitude of the forced libration. These geophysical parameters provide important constraints on the interior structure of Mercury. The measured obliquity (2.11 ± 0.1 arcmin) from the spin-axis orientation provided observational evidence that Mercury is in or very near a Cassini state [*Peale*

et al., 2002]. The large measured amplitude of the libration ($\sim$ 425 m at the equator) [*Margot et al.*, 2007; *Margot*, 2009] provided evidence that the outer solid shell of Mercury is decoupled from a liquid outer core.

After MESSENGER was inserted into orbit about Mercury in March 2011, radio tracking data led to a much improved determination of the low-degree field and the recovery of spatially resolved mass anomalies. From an analysis of the first several months of orbital data, *Smith et al.* [2012] obtained a gravity field solution to harmonic degree and order 20, which they termed HgM002. Despite strong correlations between zonal harmonics because of MESSENGER's eccentric orbit, the $\bar{C}_{20}$ value was tightly constrained, to $(-2.25 \pm 0.01) \times 10^{-5}$. $\bar{C}_{22}$ was nearly unchanged from the flyby determination, at $(1.25 \pm 0.01) \times 10^{-5}$. Modeling of interior structure was constrained by these updated values and their improved uncertainties, and led to notable changes in the understanding of Mercury's interior [*Smith et al.*, 2012]. The core fraction was revised still farther upward, and a solid FeS layer at the top of the liquid core was suggested as a means to reconcile the thin silicate shell with the large moment of inertia of the outer solid shell (to which the FeS layer would contribute). A more detailed analysis of the interior structure [*Hauck et al.*, 2013] with an updated value for the obliquity of 2.04 $\pm$ 0.08 arcmin [*Margot et al.*, 2012] showed that the FeS layer, although still allowed, is not required (see also *Rivoldini and Van Hoolst* [2013]).

1.2. The MESSENGER Mission

The MESSENGER spacecraft was launched on 3 August 2004 from Cape Canaveral. After an interplanetary trajectory more than six years long that included one flyby of Earth, two flybys of Venus, and three flybys of Mercury, a large propulsive maneuver

placed the spacecraft into a highly eccentric 12-h orbit around Mercury on 18 March 2011. During the first year of orbital operations (primary mission), the spacecraft periapsis altitude was maintained between 200 km and 500 km with regular orbit-correction maneuvers (OCMs). Spacecraft angular momentum was controlled by internal reaction wheels and commanded momentum desaturations (CMDs).

The periapsis latitude, initially at $\sim 60°$N, precessed northward to a maximum of 84.1°N in April 2013, after which the periapsis moved southward, reaching $\sim 73°$N by February 2014. The maximum altitude, over southern polar latitudes, started at $\sim 15,000$ km, a value that presents a challenge to the recovery of gravity anomalies in the southern hemisphere. After successful completion of the primary mission in March 2012 and in order to increase the frequency of observations at low altitudes, the spacecraft was placed in an 8-h orbit in April 2012, with an apoapsis altitude of $\sim$ 10,000 km. With lower fuel reserves available, the periapsis altitude was allowed to evolve naturally and drifted to higher altitudes, reaching a maximum of $\sim$ 450 km in early March 2013. Periapsis altitude is now decreasing progressively with each orbit, and an end of mission by impact onto Mercury's surface is planned for March 2015. Figure 1 summarizes the orbit evolution of MESSENGER during the orbital phase of the mission.

1.3. Outline

In Section 2, we describe the available radiometric tracking data as well as the methods used to both process the data and obtain a gravity field solution. In Section 3, we introduce the new HgM005 gravity field and describe its geophysical attributes and implications. We then discuss in detail the associated sensitivity, uncertainties, correlations, and error calibration (Section 4). We also demonstrate how we used the MESSENGER range data

to improve the ephemeris of Mercury and the experimental determination of the 3 : 2 resonance (Section 5). Finally, we show in Section 6 that near-circular frozen polar orbits are predicted to exist with the HgM005 gravity field. Such orbits could prove helpful to future exploration efforts because of lower orbit maintenance requirements and uniform global coverage.

2. Data and Methods

2.1. Data

The MESSENGER spacecraft telecommunication subsystem operates in X-band (uplink at 7.2 GHz and downlink at 8.4 GHz) [*Srinivasan et al.*, 2007], with a typical noise level equivalent to 0.1 mm/s over a 60–s integration period. Two-way and three-way radio tracking data are acquired by the NASA Deep Space Network (DSN). The radio signals are quite sensitive to plasma noise, which affects the measurement noise level. The closer the radio signal path approaches the Sun (i.e., near superior conjunction, when Mercury passes behind the Sun as viewed from Earth), the more short-lived, turbulent plasma heterogeneities produce unknown shifts in the signal frequency received by ground stations. In those geometries, with small Sun-probe-Earth (SPE) angles ($< 40°$), the signal quality can be severely degraded to the point of becoming unusable for gravity field determination.

The severe thermal environment at Mercury places important constraints on the operation of the spacecraft. A fixed ceramic-cloth sunshade protects the spacecraft bus from solar radiation and limits possible spacecraft orientation by requiring the Sun direction to be within 10° of the sunshade-normal vector. For this reason, a variety of fixed antennas are used [*Srinivasan et al.*, 2007]. Each phased-array high-gain antenna (HGA)

is collocated with a fanbeam medium-gain antenna (MGA) to provide coverage in opposite hemispheres for different Earth positions relative to Mercury. There are four low-gain antennas (LGAs) that can provide coverage when the spacecraft performs specific observations, and those are most commonly used near periapsis. For high-data-rate transmission passes, the radio-frequency system uses the fanbeam in uplink and the HGA in downlink. During these passes, the high radiometric signal levels reduce the receiver thermal noise, thus providing higher-quality tracking data (Doppler and range). Figure 2 shows that at favorable (large) SPE angles, the two HGAs have substantially better performance than the LGAs. At low SPE angles, the plasma noise dominates. Because of pointing constraints during operations, the HGAs were used mostly at high altitudes for downlink.

Near periapsis, the spacecraft must maintain the main suite of instruments in a near-nadir orientation. During slews, an apparent line-of-sight velocity of the antenna is induced by the rotation of the spacecraft. Initially we found that Doppler residuals could show high-frequency patterns, just before and after closest approach. Further analyses allowed us to relate these patterns to rapid spacecraft slews, and to recognize a discrepancy in the position of the spacecraft center of mass (COM) reported by the spacecraft guidance, navigation, and control (GNC) team compared with the reference frame of the survey of the antenna phase centers. We used the Doppler data to identify this error of $\sim$ 90 cm in relative position and further refine the center-of-mass position. Figure S1 shows the estimate of the center-of-mass position during the MESSENGER orbital phase. We adjusted the relative position of the center of mass and the antenna offsets after major OCMs, because of the larger expected shifts in COM position and absolute errors of the GNC reconstructions. Our solution is fully consistent with that of the GNC team, but it

is more accurate, with uncertainties at the mm level in each spacecraft reference frame direction. We have corrected the archived center-of-mass position information, and we note that the previous gravity solutions [*Smith et al.*, 2012; *Mazarico et al.*, 2013] were not strongly affected by this error in the center-of-mass position, because we deleted the tracking data during the most rapid spacecraft slews.

The gravity field presented here, HgM005, is an update to HgM002 [*Smith et al.*, 2012], which was based on less than 6 months of orbital data, and to HgM004, a later solution [*Mazarico et al.*, 2013] that included an additional year of data. Here, we analyzed MESSENGER radiometric tracking data acquired by the DSN from the MESSENGER spacecraft through 4 February 2014. The minimum tracking altitude achieved in the orbital phase versus position on Mercury is shown in Figure S2. In addition to measurements from the orbital mission phase, data from the three Mercury flybys are included. Notwithstanding the use of the tracking data from 2275 orbits spanning nearly 3 years, the data from the first two Mercury flybys still contribute to the determination of the equatorial gravity anomalies because of their low-altitude ($\sim$ 200 km) and near-equatorial closest approaches, compared with the $\sim$ 1000 km equatorial altitudes during the orbital phase.

A summary of the tracking data coverage and of the occurrences of spacecraft orbit maneuvers throughout the study period is given in Figure 3. MESSENGER was tracked by the DSN more extensively early in the mission. In the extended mission, only about one out of three periapsis passages was typically tracked, a schedule that yielded some one-day arcs with no data at altitudes sufficiently low to contribute to the gravity field determination.

For approximately two weeks around each of the seven superior conjunctions, the solar plasma noise was high. We did not include the weaker data from those arcs in the solution. This procedure was also followed for HgM002 [*Smith et al.*, 2012].

2.2. Methods

2.2.1. GEODYN

The orbit determination for MESSENGER has been performed using the GEODYN II orbit determination and geodetic parameter estimation software, developed and maintained at NASA GSFC [*Pavlis et al.*, 2013]. The MESSENGER tracking data were processed dynamically in 1-day segments (arcs), using a batch least-squares filter [*Montenbruck and Gill*, 2000; *Tapley et al.*, 2004]. We explicitly modeled all forces acting on the spacecraft to integrate its trajectory, and we also modeled the radiometric data observables [*Moyer*, 2003]. The arc parameters were adjusted iteratively through least squares in order to yield the smallest observation residuals (i.e., discrepancies between actual and predicted values). To limit the build-up of process noise and mismodeling errors, we reduced the arc length to no more than one day, i.e., two to three orbits, because the non-conservative forces such as that from direct solar radiation are large. MESSENGER experiences a solar flux that varies between 6.3 and 14.5 kW/m^2 over the Mercury year, a variation due to the high eccentricity (~ 0.21) of Mercury's orbit. For consistency, the arcs start and stop near apoapsis, which is convenient as it results in either two (before April 2012) or three MESSENGER orbits per arc. The full study period, March 2011 to February 2014, was divided into a total of 1058 one-day arcs.

2.2.2. General Models

GEODYN relies on a number of models to integrate the spacecraft trajectory (force models), and to determine a computed observation to be compared with the actual observable (measurement models). Here, we followed the approach outlined by *Smith et al.* [2012]. Briefly the measurement models include: troposphere refraction delays obtained from in situ meteorological data at the DSN sites, Earth orientation data supplied by the International Earth Rotation Service (IERS) [*Gambis*, 2004], ocean loading corrections for the DSN sites obtained with the GOT4.7 ocean tide model [*Ray*, 2013, Appendix A], transformations between coordinate and atomic time [*Moyer*, 1981a, b], and spacecraft antenna offset corrections obtained from the spacecraft orientation and center-of-mass position. The DSN observables have been modeled following *Moyer* [2003]. The force models include the gravitational acceleration associated with the gravity field of Mercury as given by the planetary gravitational constant, GM, the spherical harmonic coefficients, $\bar{C}_{lm}$ and $\bar{S}_{lm}$ for degree l and order m [*Kaula*, 1966], and the orientation model of Mercury; the relativistic modification of the central-body term; the third-body perturbations from major Solar System bodies computed from the DE423 planetary ephemeris [*Folkner*, 2010]; modeling of non-conservative forces such as those from solar radiation pressure and planetary radiation pressure using a spacecraft macromodel; and gravity tidal accelerations as predicted by the Love number k_2. The modeling of planetary radiation pressure includes that due to Mercury's albedo (reflected sunlight) and the planetary thermal radiation [*Mazarico et al.*, 2012; *Lemoine et al.*, 2013].

2.2.3. Non-conservative Force Models

The non-conservative forces acting on the MESSENGER spacecraft must be modeled accurately in order to recover Mercury's gravity field, tides, and rotational parameters.

The three major force models that limit the recovery of the pole orientation and tidal Love number in particular are solar, planetary albedo, and planetary thermal radiation pressures. As did *Smith et al.* [2012], we assumed a uniform surface albedo (0.074) and used a model of Mercury's surface temperature [*Paige et al.*, 2013] expanded to harmonic degree and order 4 to compute the surface thermal emission as a function of local solar time and latitude. However, because of its magnitude, the most important effect during the inversion results from the treatment of solar radiation.

The radiation pressure model consists of a shape model with twelve plates: three plates represent the sunshade, five plates the spacecraft bus (neglecting the panel behind the sunshade, as it is always occulted), and four panels for the front and back sides of the two solar panels. Telemetered quaternion data were used to orient the plates that represent the spacecraft bus, sunshade, and solar arrays. The solar panels can rotate independently from the bus, and we modeled their orientation around a gimbal as a function of time. This model explicitly includes the specular and diffusive reflectivity coefficients for each plate [*Marshall and Luthcke*, 1994].

Although we typically adjust a single parameter per arc to scale the three radiation accelerations, we find that the mismodeling of the radiation pressures can be better accommodated during arc convergence by estimating the areas of the 12 spacecraft plates. These areas generally increase the modeled spacecraft area by ∼15–20% when the MESSENGER orbit is in a noon-midnight configuration. In many instances, it is reduced, by up to ∼10%, presumably due to self-shadowing effects not computed here [*Mazarico et al.*, 2009]. During the global inversion of the solution, we kept the areas fixed to the values adjusted during orbit determination, but we estimated the sunshade and solar

panel reflectivities. The corrections to the *a priori* values are small, except for the diffuse reflectivity of the solar panel. We attribute this larger magnitude to the large thermal reradiation this panel must emit because of its high temperature, an effect not yet modeled in our work for MESSENGER, unlike the treatment by *Antreasian and Rosborough* [1992] and *Marshall and Luthcke* [1994] for TOPEX/Poseidon. The estimation of the plate areas during the orbit determination process and of the reflectivities in the global iteration help alleviate such model shortcomings. When spacecraft areas and reflectivities are not corrected, the radiometric data fits worsen, and the estimates of the Love number k_2 and the obliquity are affected. Some of the changes in the low-degree field compared with HgM002 can also be attributed to the improved force modeling presented here.

2.2.4. Planetary Orientation

A gravity field model is inextricably linked to the definition of a model for planetary orientation. In the absence of a good orientation model, the position of gravity anomalies would not appear fixed over several Mercury rotations, and the anomaly estimate would be compromised. The orientation parameters can be considered force model parameters, as they affect the inertial trajectory of the satellite, which is the basis of estimation. The orientation parameters are also critical to ascertain the state of the interior of the planet (Section 3.6). *Margot et al.* [2007] determined an orientation model of Mercury from ground-based radar measurements, adding a non-zero obliquity and periodic longitudinal librations to the existing International Astronomical Union (IAU) model [*Davies et al.*, 1980]. *Margot* [2009] and *Margot et al.* [2012] further refined those parameters, with a libration amplitude at the equator of $\sim$ 450 m. We used their prime meridian to define the principal axes (PA) frame in which the gravity field is best expressed, rather than the

IAU prime meridian that was chosen to maintain the Hun Kal crater at a longitude of −20°E. In this PA frame, the $\bar{C}_{21}$, $\bar{S}_{21}$, and $\bar{S}_{22}$ coefficients are expected to be close to zero.

For MESSENGER's orbital mission phase, the project adopted the JPL DE423 ephemeris [*Folkner*, 2010] for mission planning and archived data products, and the gravity fields produced from MESSENGER data have been based on arcs reconstructed with that ephemeris. Recently, *Folkner et al.* [2014] produced a new Solar System ephemerides solution, DE430. Although we did not use the newer solution to produce HgM005, we evaluated it with the range data, and we found a clear improvement in terms of range residuals. In Section 5, we discuss the Mercury ephemeris and its estimation.

2.2.5. Solution Strategy

Each converged arc was processed in GEODYN to create normal equations, which were used to produce the gravity solution. In addition to arc-specific parameters, each arc's normal equation contains the 2,597 Stokes coefficients ($\bar{C}_{lm}$ for a degree and order 50 gravity field, $\bar{S}_{lm}$), but also a suite of other global (common) parameters: the spacecraft low-gain antenna position correction, the spacecraft reflectivity parameters, the tidal Love number k_2, the Mercury orientation parameters (right ascension, declination, and spin rate), and the Mercury gravitational parameter (GM). The antenna location adjustments are then tied together to correspond to a shift in the estimate of center-of-mass position.

For the global solution, each converged arc was weighted according to its post-convergence observation residuals. In intermediary global solutions (predecessors to HgM005), arcs were weighted $\sim$ 30% lower than their root mean squared (RMS) level;

the factor for HgM005 was 10%. This weighting scheme allows arcs of varying quality to contribute to the solution appropriately.

The HgM005 gravity field is based on 632 orbital arcs, out of the original 1058 arcs covering the study period. The former figure constitutes a substantial down-selection, but we found it beneficial to the overall solution. Although *Smith et al.* [2012] could not be as selective for HgM002 because of the short data span, now that we have about three years of orbital tracking data, we can select only the best-determined and most sensitive arcs without sacrificing broad spatial coverage.

Because of solar plasma effects, we did not consider 337 arcs with low SPE angle ($< 40°$). We also excluded all the arcs with any kind of spacecraft maneuver, specifically 132 arcs over the three years of orbital observations. The total number of arcs removed was 426, accounting for the fact that some maneuvers occurred near superior solar conjunctions. Four of the remaining arcs were also deleted due to higher-than-normal residual RMS (> 1 mm/s).

The normal equations were formed from each individual arc with GEODYN, and then merged with a degree power law (or Kaula) constraint equation before inversion using GEODYN's companion program SOLVE [*Pavlis et al.*, 2013]. The constraint is necessary to ensure the stability of the solution, given that the expansion degree is larger than what the data alone can support globally (especially in the southern hemisphere); this point is discussed in detail in Section 4.1. Although we experimented with a variety of strategies (e.g., the choice of parameters to estimate), the solution presented here uses an inversion approach for the global parameters similar to *Smith et al.* [2012]. Specular and diffuse reflectivity parameters for the solar arrays and specular reflectivity for the sunshade were

carried through to the final least-squares inversion; the other arc parameters were back-substituted during the combination of each arc's normal equation.

3. The HgM005 Solution, and Geophysical Implications

3.1. Gravity Anomalies and Mascons

The free air gravity anomaly field of the HgM005 gravity model is shown in map view in Figure 4, in both Mercator and polar stereographic projections. The map is visually very similar to those of *Smith et al.* [2012] and *Mazarico et al.* [2013] (Figure S3), despite the additional years of data. However, in HgM005 large-scale anomalies have greater confidence, and additional shorter-wavelength signals are present because of the harmonic expansion to degree and order 50.

The most prominent features in the gravity anomaly map (Figure 4) are the large positive anomalies, over the northern rise ($\sim 70°N$, $35°E$), over the Caloris basin ($\sim 30°N$, $160°E$), and near the Sobkou basin ($\sim 35°N$, $225°E$). These features have been discussed by *Smith et al.* [2012]. As they argued, although only the Caloris anomaly is directly associated with an impact basin, the Budh-Sobkou anomaly may also qualify as a basin-associated mass concentration, or mascon, because it is a gravity high and is associated with an elevated crust-mantle boundary in crustal thickness models. Several apparently continuous linear features appear in Figure 4, such as one between ($\sim 10°N$, $60°E$) and ($\sim 30°N$, $140°E$). These linear features are correlated with topography, but they are relatively subdued in power, indicating that the topographic variations might be isostatically compensated. We present an updated crustal thickness map in Section 3.3.

3.2. Correlation with Topography

As the Gravity Recovery and Interior Laboratory (GRAIL) mission demonstrated to extraordinarily high resolution at the Moon [*Zuber et al.*, 2013], gravity and topography are expected to be correlated, particularly at shorter wavelengths, because surface relief contributes to the planet's gravitational potential. However, at the longest wavelengths (low degree and order), such a correlation does not necessarily hold because of isostatic compensation as well as uncompensated subsurface mass anomalies in the crust and mantle. The gravitational signature of structures at depth is attenuated at orbital altitudes and can be detected only as long-wavelength signals. As on the Moon, in the spectral range of the HgM005 gravity field (harmonic degree $l = 2 - 50$), we do not expect the gravity and the topography to be fully correlated. Nonetheless, higher correlation values have typically been taken as indicators of gravity field improvement, in the case of Mars [*Konopliv et al.*, 2011] and the Moon [*Zuber et al.*, 2013].

We computed the global correlation of the gravity field with a global topography model. *Smith* [2014] archived in the NASA Planetary Data System (PDS) a spherical harmonic expansion of Mercury's topography to degree and order 120 for a solution that combines Mercury Laser Altimeter (MLA) measurements [*Zuber et al.*, 2012] and radio occultation measurements [*Perry et al.*, 2013]. Because MLA cannot obtain measurements at ranges greater than $\sim$ 1800 km, the occultation-derived radii, although limited in precision and spatial coverage, are critically important to define the long-wavelength shape of the southern hemisphere. However, in the northern hemisphere, the topography is not the limiting error source, as the density of MLA measurements is sufficient at the resolution of the gravity field in our analysis. As shown in Figure 5, the correlations for $l < 20$ (see Section 4.3) are typically ~ 0.6. This correlation is reasonably high given the challenges posed

by the eccentric orbit of MESSENGER. HgM005 has higher correlation values than the earlier HgM002 and HgM004 solutions, more markedly at $l > 10$ (Figure 5). For degrees greater than $l = 20$, the correlations steadily decrease to < 0.2 for $l > 35$, as expected from the degree strength (Section 4.3). This comparison indicates that the resolution of the gravity anomaly field in the southern hemisphere is low. This inference is further demonstrated in the lower panel of Figure 5, where we show localized correlations, computed following *Wieczorek and Simons* [2005]. These correlation values, after localization with a windowing width of either $l_{win} = 2$ or $l_{win} = 5$ for a cap of half-angle 30°, are higher than the global values, typically $0.6 - 0.8$ for $l = 5 - 15$. The higher correlation values over $l = 25 - 35$ are also indicative of better-resolved gravity anomalies for the northernmost latitudes.

3.3. Bouguer Gravity Anomaly and Crustal Thickness

With the same topographic model as that used in Section 3.2 for the correlation of gravity and topography, we computed the gravity expected from the topography. We assumed a uniform density for the crust $\rho = 3200$ kg m^{-3} [*Smith et al.*, 2012], and we made use of the finite-amplitude method of *Wieczorek and Phillips* [1998] up to degree and order 5.

The topography model has much higher intrinsic resolution than the gravity model, especially at lower latitudes. In order to be compatible with the spatial scales resolved by the HgM005 gravity field, we therefore limited the resolution of the topography field by expanding a spherical harmonic representation only up to low degrees. This procedure effectively filters out shorter-wavelength features. We found, however, that a single degree for truncating the expansion is not optimal. A truncation at $l = 20$ is adequate near the

equator, but such a limit is too severe at high northern latitudes, where HgM005 resolves shorter-wavelength structure. A truncation at $l = 50$ is more suitable for the north polar region, but it yields more features and power at lower latitudes than the gravity field can resolve. To construct the gravity field from topography shown in Figure 6a, we expanded the gravitational potential from topography to a degree consistent with the resolution of the gravity field at that location, as specified by the HgM005 degree strength (cf. Section 4.3). We then subtracted the topography-derived gravity from the measured HgM005 gravity field to obtain the HgM005 Bouguer gravity anomaly field (Figure 6b). At the northernmost latitudes, several features in the free air gravity anomaly and Bouguer correction maps are not seen in the Bouguer anomaly field, indicating a lack of compensation. This effect is notably the case for the northern rise mentioned above.

Under the assumption of Airy isostasy, the Bouguer anomalies are indicative of variations in the depth of the crust-mantle boundary, and the Bouguer map can be translated into a map of crustal thickness (Figure 6c). Following *Smith et al.* [2012], we assumed an average crustal thickness of 50 km and a crust-mantle density contrast of 250 kg m^{-3}. The equatorial and polar regions are characterized by thicker and thinner crust than average, respectively. Such long-wavelength variations in apparent crustal thickness might also have contributions from variations in crustal or mantle density.

3.4. Low-degree Field

As noted above, the low-degree coefficients in the gravity field are important both for understanding the structure of Mercury's interior and for modeling the long-term evolution of a spacecraft orbit. The HgM005 $\bar{C}_{20}$ and $\bar{C}_{22}$ values are in good agreement with the HgM002 values of *Smith et al.* [2012], having changed respectively by 0.22% and

0.67%, figures less than the standard deviation of 0.01×10^{-5} (i.e., 0.44% and 0.80%, respectively) in the HgM002 solution. The differences with respect to HgM004 are even smaller (0.05% and 0.27%, respectively), indicating the robustness of these estimates with increased temporal coverage. However, larger discrepancies ($6 - 9\%$) exist for the $\bar{C}_{30}$, $\bar{C}_{40}$, and higher-degree zonal coefficients, which are highly correlated (Section 4.5). The HgM005 values are closer to the estimates of *Genova et al.* [2013] than to the HgM002 values. We ascribe those changes to a more careful consideration of the antenna phase offset corrections and of the parameters associated with solar radiation (area scale factors and panel reflectivities), as described in Section 2.2.1. These changes are particularly relevant to the orbit evolution of the Mercury Planetary Orbiter of the BepiColombo mission now in development by the European Space Agency and the Japan Aerospace Exploration Agency, as discussed by *Genova et al.* [2013].

The gravitational parameter of Mercury (GM) also differs from previous estimates, at $2.2031870799 \times 10^{13} \pm 8.6 \times 10^{5}$ m^3 s^{-2} (after calibration, see Section 4.4). Although the changes from HgM002 and HgM004 ($\sim 9 \times 10^7$ and $\sim 3 \times 10^7$ m^3 s^{-2} respectively) are small in absolute terms, they are significant compared with the formal uncertainties. Again, this improvement is likely due to improved (reduced) correlations with the solar radiation and the spacecraft state-vector parameters. The HgM005 value of GM is in good agreement with the navigation team determination (difference of $\sim 1 \times 10^7$ m^{3}s^{-2}), especially when compared with the estimates from *Anderson et al.* [1987] and *Genova et al.* [2013] (with differences of approximately -22×10^7 and -19×10^7 m^3 s^{-2}, respectively).

3.5. Tidal Love Number k_2

The tidal Love number k_2 describes the amplitude of the time-variable degree-2 gravity signal due to the tides raised by the Sun on Mercury. In addition to its direct effect on the trajectory of MESSENGER, it can provide constraints on the internal structure of Mercury [*Van Hoolst and Jacobs*, 2003; *Van Hoolst et al.*, 2007; *Rivoldini et al.*, 2009; *Padovan et al.*, 2014], beyond those imposed by the moment of inertia and obliquity [*Peale et al.*, 2002; *Margot et al.*, 2012; *Hauck et al.*, 2013]. The parameter is particularly sensitive to the core size and outer solid shell thickness, and it also varies with the rigidity and temperature of the mantle layer, as illustrated by *Padovan et al.* [2014]. The HgM005 solution for the tidal Love number, $k_2 = 0.451 \pm 0.014$ (after scaling by a calibration factor of 10, see Section 4.4), is the first obtained directly from observations. We note that our value depends on the specific modeling and inversion strategy of the radiation pressure accelerations. Accounting for possible systematic effects and biases, a wider range of $k_2 = 0.43$–0.50 can thus not be ruled out with our HgM005 solution.

We used the ALMA modeling tool [*Spada*, 2008] to calculate the k_2 value expected from models of internal structure. Following *Smith et al.* [2012] and *Hauck et al.* [2013], we varied the thickness of the lithosphere between 70 and 90 km and the rigidity of both the lithosphere and a possible solid FeS layer (between the mantle and the fluid core). The resulting k_2 values (Table 1) range between 0.46 and 0.62. The range is consistent with that of *Van Hoolst and Jacobs* [2003] and *Rivoldini et al.* [2009], who suggested a value of 0.4–0.6 prior to the MESSENGER mission. We note that the larger values ($k_2 > 0.5$) are obtained only when assuming that a solid FeS layer is present. Initially proposed by *Smith et al.* [2012] to account for the large moment of inertia of the solid outer shell, as noted above, an updated analysis by *Hauck et al.* [2013] with the latest obliquity values

[*Margot et al.*, 2012] found that such a layer, although still compatible with the data, is no longer required, in agreement with the findings of *Rivoldini and Van Hoolst* [2013].

More recently, *Padovan et al.* [2014] explored the tidal Love number with a rheological model and a large range of governing parameters to find solutions compatible with the MESSENGER and ground-based geophysical observations [*Hauck et al.*, 2013]. Although somewhat extreme scenarios with very high rigidities can produce low k_2 values as low as 0.4, *Padovan et al.* [2014] obtained a range of 0.45–0.52 for a mantle grain size of 1 cm. Smaller grain sizes (1 mm) would result in larger values (by $\sim 10\%$). Our estimate of k_2 from the gravity field solution is fully consistent with their results, leaning slightly toward the lower values.

The k_2 value obtained from MESSENGER tracking data, although still considered preliminary, is fully consistent with model expectations built from the earlier gravity results of *Smith et al.* [2012]. As additional gravitational data are acquired by MESSENGER, increasingly refined estimates of k_2 will help to further constrain the interior structure and rheology of Mercury's interior.

3.6. Mercury Orientation: Pole Position, Obliquity, and Spin

With less than 6 months of data, i.e., less than 3 Mercury spin periods, *Smith et al.* [2012] did not attempt to estimate Mercury's orientation parameters along with the HgM002 gravity field. For the HgM005 solution, in contrast, we estimated the right ascension (RA) and declination (DEC) of the pole and the spin rate. We prepared an alternate solution for which we also adjusted the amplitude of the longitudinal librations, but our current sensitivity to that parameter with current radio tracking data is limited.

Because the pole parameters are connected to the $\bar{C}_{21}$, $\bar{S}_{21}$, and $\bar{S}_{22}$ terms, small estimated values for these coefficients are indicative of good recovery of pole parameters, because the expected values of these coefficients in the PA frame are zero. As shown in Table 3, we do obtain suitably low values for those coefficients. We note that the $\bar{C}_{22}$ and $\bar{S}_{22}$ values may indicate a shift of the principal axes frame in longitude of $\delta\phi_{PA} = arctan(\bar{S}_{22}/\bar{C}_{22})/2 \sim -0.048°$, equivalent to $\sim$ 2 km at the equator. Use of the IAU convention for the prime meridian [*Archinal et al.*, 2011] would result in a substantially larger value of $\bar{S}_{22}$.

Our updated pole position at J2000 is $RA = 281.00480° \pm 0.0054$ and $DEC = 61.41436° \pm 0.0021$ (after calibration, see Section 4.4), approximately 10 arcseconds away from the best-fit position of *Margot et al.* [2012] which we used as an a priori estimate in our solution. From these values, we computed the obliquity, the angle between Mercury's orbit plane normal and its spin axis. *Margot* [2009] obtained an obliquity of 2.11 $\pm$ 0.10 arcmin. With improved modeling and additional ground-based radar observations, *Margot et al.* [2012] refined the spin axis orientation ($RA = 281.0103°$, $DEC = 61.4155°$) and revised their obliquity estimate to 2.04 $\pm$ 0.08 arcmin. The HgM005 solution yields an obliquity of 2.06 $\pm$ 0.16 arcmin (calibrated uncertainty). This value is entirely consistent with both the *Margot* [2009] and *Margot et al.* [2012] estimates (within half a standard deviation).

From the $\bar{C}_{20}$ and $\bar{C}_{22}$ values and this obliquity (with an uncertainty equal to the formal error multiplied by 5), we obtain an estimate of the polar moment of inertia $C/MR^2 = 0.349 \pm 0.014$, where R is Mercury's mean radius. The fractional part due to the solid outer shell is $\bar{C}_m/C = 0.424 \pm 0.024$. These values are only slightly different from

those of *Margot et al.* [2012] (larger by 0.2 and 0.25 standard deviations, respectively). Such small changes are compatible with the majority of the interior structure models presented by *Hauck et al.* [2013]. Compared with their nominal model, our updated values imply a slight decrease in the outer shell thickness (by $\sim$ 15 km), an increase in the outer shell density (by $\sim$ 54 kg m^{-3}), and an increase in the density of the innermost solid and outer liquid cores (by $\sim$ 115 kg m^{-3}).

With Mercury in a 3:2 spin-orbit resonance, its spin rate (except for the effect of librations) is directly tied to Mercury's orbital period (around the Sun). We obtain a spin rate correction relative to the IAU convention (a spin period of 58.646220 days) [*Archinal et al.*, 2011] of (9.042 $\pm$ 1.288) $\times$ 10^{-11} degree s^{-1}, or a corrected period of 58.646146 $\pm$ 0.000011 days. In addition to the good sensitivity of the MESSENGER observations over nearly 20 spin periods, this change is justified by the improved consistency with the 3:2 resonance when combined with the orbital period (Section 5). The IAU convention does not include an uncertainty, but our new estimate is consistent with the spin period of *Klaasen* [1976] (58.6461 $\pm$ 0.005 days). In Section 5, we discuss the adjustment of the Mercury ephemeris, which can be used as a further check on this updated rotation period, because of the 3:2 spin-orbit resonance.

4. Sensitivity Analysis

In this section, we evaluate the quality, sensitivity, and uncertainties of the HgM005 gravity field. We first justify our choice of the regularization constraint to stabilize the gravitational anomalies in the southern hemisphere (Section 4.1). We then propagate the covariance matrix obtained during the least-squares inversion to spatially map the expected error levels in the anomaly map (Section 4.2), and we construct a degree strength

map describing the spatial resolution of HgM005 (Section 4.3). We determine a scale factor to calibrate the formal uncertainties to more conservative values (Section 4.4), and we evaluate the correlation between estimated parameters, in particular the zonal terms (Section 4.5).

4.1. Kaula Constraint

Regularization is required since the solution is being expanded to a spherical harmonic degree that the data do not support on a global basis, because of a strong variation of altitude with latitude.

An *a priori* constraint on the magnitude of the Stokes coefficients is necessary for the determination of spherical harmonic gravity field solutions if the data are not globally distributed at the wavelength of the truncation degree. In the determination of planetary gravity fields, the "Kaula rule" is used for a smoothing constraint, whereby each coefficient $\bar{C}_{lm}$ or $\bar{S}_{lm}$ is assigned an *a priori* uncertainty on the basis of its expected variance at degree l [*Kaula*, 1966]. Empirically, this constraint follows a $1/l^2$ relationship, which can be justified *a priori* by the self-similar fractal nature of planetary surfaces and *a posteriori* by the gravity power spectra of Earth [*Lemoine et al.*, 1998], Mars [*Lemoine et al.*, 1997], and the Moon [*Lemoine et al.*, 2013]. The strength of the constraint is given by a scaling factor K, for an expected RMS power of K/l^2. Each planetary body has its own Kaula scale factor. Through scaling relationships from other bodies [*Konopliv et al.*, 2014], we would expect $K \sim 4$–5×10^{-5} for Mercury (Table 2).

The RMS power $\left(P_l = \sqrt{(2l+1)^{-1} \times \sum_m (\bar{C}_{lm}^2 + \bar{S}_{lm}^2)}\right)$ of HgM005 presented in Figure 7 does match the $K \sim 4 \times 10^{-5}$ rule reasonably well at low degrees, indicating that the "true" level of the Kaula factor may be close to that number. Unfortunately, because

of MESSENGER's eccentric orbit, use of this Kaula factor globally leads to implausible gravity anomalies in the southern hemisphere. We therefore chose a stronger Kaula constraint, $K = 1.25 \times 10^{-5}$, as it prevents large anomalies from developing in the southern latitudes without overly smoothing the solution in the north. We found that strengthening the constraint further is detrimental, as it smoothes the field nearly equally in the south and in the north.

Because a consequence of the Kaula constraint is to bias each coefficient toward zero, we prepared low-degree solutions with no Kaula constraint in order to ascertain that the low-degree field is generally not affected by its application. The low-degree field is especially important for interior modeling [*Hauck et al.*, 2013] and calculations of spacecraft orbit evolution [*Genova et al.*, 2013]. We obtained alternate solutions with no Kaula constraint, and with increasing truncation degrees up to $l = 20$. These unconstrained solutions are themselves strongly degraded, because of truncation aliasing (for the $l = 4$–5 solutions) and instabilities leading to large power at the higher degrees (for the $l = 7$–20 solutions). Nonetheless, the RMS power of these unconstrained solutions indicates that the HgM005 solution is not driven to a lower power because of the Kaula constraint (Figure 7). As an additional precaution, we applied the Kaula rule only above $l = 7$ for HgM005, whereas *Smith et al.* [2012] applied the Kaula constraint starting at degree $l = 3$. However, we note that the differences from a solution constrained from $l = 2$ are very small, with the RMS power of the differences lying below the formal error spectrum. These unconstrained solutions also show that without regularization the MESSENGER data can determine a gravity field only to degree and order 6. Comparison of gravity anomalies expanded to

$l = 15$ with those obtained with a stronger constraint ($K = 4.0 \times 10^{-5}$) shows small differences in the northern hemisphere, below 2 mGal RMS.

At high degrees ($l > 20$), the power drops markedly, to approach the level of the $K = 1.25 \times 10^{-5}$ rule. We interpret this behavior to signify that the data can partially support a degree $l = 15$–20 field, as the power up to $l = 20$ stands high despite the chosen Kaula rule. The Kaula constraint drives the global power levels at shorter wavelength ($l > 20$), because the data are sensitive only to anomalies at the northernmost latitudes. Thus, we select $K = 1.25 \times 10^{-5}$ for its effect at high degrees, where it is necessary, rather than for its validity at long wavelengths, where it is less needed. More refined approaches exist and could be explored for Mercury, such as spatial-spectral constraints [*Konopliv et al.*, 1999] or localized Kaula constraints [*Han et al.*, 2009; *Mazarico et al.*, 2010], but such efforts are beyond the scope of this paper.

As we explained above, we recognize that the total field power may be over-constrained by the stronger Kaula factor, and we expect the true gravity field power to follow a $K \sim 4 \times 10^{-5}$ rule. We justify our choice because for the primary purposes of HgM005, including global geophysical analysis, we want to prevent large but poorly constrained anomalies in the southern hemisphere. Future low-altitude data from MESSENGER or other spacecraft will be important in refining the gravity field.

4.2. Covariance Error Analysis

The projected formal errors for the gravity anomaly field for the HgM005 model, as calculated from the full error covariance matrix, are shown in Figure 8a. The formal errors range between 2.5 and 8.5 mGal and vary predominantly with latitude because of the eccentric orbit of MESSENGER. Comparison with earlier fields (HgM002, HgM004)

shows typical 2–4 mGal RMS differences northward of 20°N, in good agreement with the propagated errors. In the southern hemisphere, RMS differences range from 6 to 18 mGal with an average of 10 mGal, indicating that the formal errors underestimate uncertainties at those latitudes. The low-altitude flyby passes positively influence the projected errors near the equator. We also calculated the errors from only those coefficients up to $l = 20$. The northern hemisphere anomaly errors at those longer wavelengths are much smaller, a result that is consistent with the error power spectrum in Figure 7 reaching a noise-to-signal ratio near unity around $l = 25 - 35$. In the south, where the Kaula constraint is more effective in reducing the power of the shorter wavelengths, the error level is not decreased as appreciably and is still much higher than in the north.

Taking into account the calibration factor discussed below, it might be possible that gravity anomalies as large as 60–80 mGal, and not confined to short wavelengths, could remain undetected at southern latitudes.

4.3. Degree Strength

An extension of this spatial covariance error propagation is the degree strength map, illustrated for Venus by *Konopliv et al.* [1999] and for the Moon by *Konopliv et al.* [2013]. The idea is to obtain, for each point on the globe, the degree at which the anomaly error calculated from the covariance matrix is equal to the expected anomaly given that the gravity coefficients follow the Kaula constraint precisely, that is, when the signal-to-noise ratio at that point is equal to unity (as illustrated in Figure S5). Clearly, the resulting map, shown in Figure 8b, has a zonal pattern because of MESSENGER's eccentric orbit, much like the anomaly error map. The minimum degree strength is found in the south polar region, where $l_{strength} \sim 8$, and the maximum $l_{strength} \sim 36$ is near the north pole.

Near the equator, the degree strength is $\sim$ 15 corresponding to a resolution of $\sim$ 500 km on the surface, which is perhaps optimistic despite the two short tracked segments of the flybys given that the spacecraft altitude over the equator is generally $\sim$ 1000 km. A degree strength of 35–36 near the north pole is in line with the expected resolution given spacecraft altitudes above 200 km.

The degree strength is useful in gauging the extent to which the anomaly map can be used with confidence for geophysical interpretation at a given location. To illustrate this point, we used the degree strength map to create an anomaly map expanded at each point only up to its specific degree strength. Figure 8c presents this "degree strength anomaly map," which is smoother than the full expansion of HgM005 (Figure 4) in the northern hemisphere and slightly damped near the equator. However, it is better resolved than the $l = 20$ expansion of HgM005 (and HgM002), as its degree strength reaches $\sim$ 36.

4.4. Error Calibration

Smith et al. [2012] scaled the formal uncertainties for HgM002 on the basis of their understanding of the confidence level that could be assigned to the low-degree coefficients. In particular, the quoted 0.01×10^{-5} uncertainty for the $l = 2$ coefficients reconciled the magnitude of the $\bar{C}_{21}$, $\bar{S}_{21}$, and $\bar{S}_{22}$ coefficients with their expected zero values in the principal axes frame. We use the same argument (Table 3).

The HgM005 low-degree formal uncertainties are smaller by a factor of $\sim$ 5 than those for HgM002. We also consider the magnitude of the gravity anomaly error implied spatially by the HgM005 covariance matrix (Section 4.2): given the existence of $\sim$ 120 mGal gravity anomalies in the northern hemisphere, and the expectation that some unresolved

or indiscernible anomalies of similar magnitude might exist in the southern hemisphere, uncertainties of 80 mGal or more in that region are appropriate.

As a result, we recommend a scale factor of 10 to 15 to obtain conservative error estimates for the gravity field coefficients. This recommendation translates to a scaled uncertainty of 0.001×10^{-5} on the $\bar{C}_{20}$ and $\bar{C}_{22}$ coefficients, still a ten-fold improvement relative to HgM002. The tidal and rotational parameters, because of their long wavelength and global scale, do not suffer from the same loss of sensitivity because of orbit geometry, and we do not apply a scaling of the formal uncertainties.

4.5. Low-degree Coefficient Correlations

As noted by *Smith et al.* [2012], the low-degree zonal coefficients are highly correlated. Due to the nature of their perturbations, neighboring zonals are anti-correlated, but the correlation coefficients rapidly decrease with a mismatch between degree and/or order (see Figure S4). The slow rotation of Mercury and the short arc duration chosen because of force mismodeling concerns make the sampling of the resonances due to the zonal terms difficult (for example, the spacecraft initial state is estimated daily), and we can observe only a lumped effect. This effect is, however, not limited to zonals, as $\bar{C}_{lm}$ or $\bar{S}_{lm}$ coefficients of the same order m exhibit this behavior, which is expected as such terms produce perturbations at the same frequencies [*Kaula*, 1966].

The additional data included in HgM005 compared with HgM002 did not alleviate this behavior, but the improved force modeling and inversion strategies of arc selection and arc weighting helped reduce the strongest correlations. For example, the correlation between $\bar{C}_{20}$ and $\bar{C}_{30}$ decreased from -0.86 to -0.67. This decreased correlation adds confidence to the determination of the $\bar{C}_{30}$ coefficient, important for long-term orbit evolution (Sec-

tion 6). Future improvements may be obtained when performing the orbit determination over longer arcs, and of course once other spacecraft are placed into different orbits around Mercury, such as BepiColombo [*Iess et al.*, 2009].

5. Mercury's Ephemeris and 3: 2 Resonance

The range measurements to MESSENGER, although not contributing as much as the range rate to the gravity field solution, are directly sensitive to errors in the modeled position of the planet, or ephemeris error. Figure 9 shows the pass-by-pass range biases estimated after convergence of the one-day arcs with the MESSENGER radio tracking data given the starting DE423 ephemeris. The periodic variations indicate Mercury position errors. Whereas the DE423 and DE430 planetary ephemerides result from a combined trajectory adjustment of the full Solar System (i.e., hundreds of major and minor planetary bodies), in this work we attempt only to adjust the orbital elements of Mercury itself. With the more recent DE430 ephemeris (which includes some MESSENGER data) [*Folkner et al.*, 2014]), the higher-frequency errors are significantly reduced: the RMS of the range residuals outside of the low-SPE-angle periods decreases from 57.8 m to 24.4 m (Figure 9).

After having obtained the HgM005 solution, we re-converged the data arcs with our new gravity field. We used the residuals of the range data over the full mission to estimate a relative correction at J2000 to the trajectory of Mercury, with the "Set III" formulation of *Brouwer and Clemence* [1961] (Table 4). We then reprocessed the data arcs with these corrections. We find significant improvements with this linear correction in J2000 compared with both the starting ephemeris DE423 and the DE430 solution, with a range residual RMS of 10.9 m (Figure 9). In-plane corrections are $\sim$ 50 m. Out-of-plane

corrections are larger, about 1 km, but we note that the cross-track (inclination) direction is not as well constrained from ground-based radio tracking. The incorporation of a long time series of Earth-MESSENGER range measurements will likely improve the quality of the Solar System and Mercury ephemerides further. We note that *Verma et al.* [2014] recently improved their Solar System ephemeris using MESSENGER tracking data and obtained a similar level of post-fit range residuals (2.8 ± 12.0 m with data up to September 2012).

Our correction also yields an updated semi-major axis of Mercury, which can be converted to an orbital period around the Sun, to which we add ~ 8 s to account for the precession of the longitude of the perihelion [*Shapiro*, 1989]. We find $P_{orbit} = 87.969216879$ days $\pm$ 6 s. In combination with our new spin period estimate of $P_{spin} = 58.646146 \pm 0.000011$ days (Section 3.6), we find a ratio P_{orbit}/P_{spin} of 1.49999900. This ratio is a factor of ~ 2 closer to the expected 3: 2 ratio than for our *a priori* models (the orientation parameters of *Margot et al.* [2012] and the DE423 ephemeris), with the discrepancy decreasing from $\sim 3.5 \times 10^{-6}$ to $\sim 1.0 \times 10^{-6}$, and it provides further and more accurate experimental determination of Mercury's lock in the 3: 2 resonance. It also demonstrates the quality of our two independent measurements of Mercury's spin rate and ephemeris.

6. Future Mission Planning, and BepiColombo

With confidence in the low-degree gravity field, it is possible to consider whether there are certain classes of orbits that are particularly advantageous for future Mercury orbital missions. Although planning for the next mission to Mercury, the dual BepiColombo orbiters, is too far advanced to benefit from this analysis, the exercise is more than of academic interest. Indeed, the MESSENGER mission lifetime was restricted by the amount

of propellant available after orbit insertion. So-called "near-frozen" orbits, defined as orbits for which the elements are nearly constant when averaged over a finite time interval, offer a cost-saving alternative to the frequent orbit-correction maneuvers MESSENGER employed to manage periapsis altitude and delay impact.

Previous work on frozen orbits around Mercury include the analyses by *Delsate et al.* [2010] and *Ma and Li* [2013], but we note that those studies did not benefit from or make use of the recent MESSENGER gravity results. They also considered only the $\bar{C}_{20}$ and $\bar{C}_{30}$ coefficients, although we note that they focused on highly eccentric orbits. In those cases, the perturbations by the gravitational attraction of the Sun dominate, along with the secular changes resulting from $\bar{C}_{20}$ and $\bar{C}_{30}$. Here, we concentrate on near-circular frozen orbits, following *Cook* [1991], and we initially consider all the zonal coefficients of HgM005, i.e., up to degree 50. We perform a search for frozen orbits for different semi-major axis values over all values of inclination i from 0° to 180°. For each case, we obtain a frozen eccentricity. We find that the frozen eccentricity converges after inclusion of terms through degree $l = 15 - 25$, depending on the altitude considered. This relatively high-convergence degree may be a consequence of the high correlation of the zonal terms (Section 4.5). We note that the secular effects of the zonal terms decrease with degree and altitude, and that the power of the HgM005 zonals at high degree is dampened by the Kaula constraint. Nonetheless, it appears that $\bar{C}_{20}$ and $\bar{C}_{30}$ are not sufficient to predict the frozen eccentricity.

The results of our calculations for an average altitude h of 300, 500, and 1000 km are show in Figure 10. The maximum allowable eccentricity (i.e., the eccentricity that would lead to a periapsis equal to the reference radius $R = 2440$ km) is, respectively, $e_{max} = 0.11$,

0.17, and 0.29. Frozen orbits exist for many of these inclinations and semi-major axis values. Outside of a narrow range ($i = 65 - 70°$), the periapses are typically near the south pole (argument of pericenter $\omega = 270°$), as in the case of the Moon (for instance, the orbit chosen for the Lunar Reconnaissance Orbiter during its commissioning and extended mission phases [*Chin et al.*, 2007]). Over a wide range of moderate inclinations ($i = 30 - 60°$ prograde and retrograde), low-eccentricity frozen orbits are possible. For $h = 1000$ km, near-equatorial and near-circular frozen orbits exist. However, we focus here on the polar orbits, which are most interesting for a potential future orbiter mission, as they would provide global coverage.

Because the Sun exerts a large third-body perturbation at Mercury and dominates orbit evolution for MESSENGER, we used GEODYN to perform a high-fidelity orbit propagation of the $h = 500$ km polar orbit, with the full (degree and order 50) HgM005 gravity field (in contrast to the initial search discussed above for which only zonal terms were considered). In addition to the gravitational acceleration from the Sun, we also considered additional perturbations such as the direct solar radiation pressure and the planetary thermal and albedo radiation pressure accelerations. Figure 11a shows the evolution of this $h = 500$ km polar orbit over 8.5 years in terms of equinoctial elements, a phase space used to evaluate orbit stability: $esin(\omega)$ versus $ecos(\omega)$. The stability of the orbital elements is clear despite their complicated pattern, and no long-term drift exists. The periapsis altitude is also very stable (Figure 11b), varying only by ~ 12 km over the 8.5-year orbit integration.

In order to consider the impact of the HgM005 uncertainties in our calculations, we performed those computations again, with 25 so-called "clone fields." Each clone repre-

sents an alternative solution to the least-squares inversion, consistent with the covariance matrix. Varying each coefficient according to its individual uncertainty would not be appropriate, as doing so ignores the correlations between coefficients and would thus not statistically replicate the initial field. Instead, we construct the clone fields from the covariance matrix, which precisely accounts for the error characteristics of the HgM005 gravity model. As described in the supplementary material of *Smith et al.* [2012], the covariance matrix was first diagonalized. Then each eigenvector was scaled by the square root of its eigenvalue and a random factor, and finally the eigenvector was added to the baseline solution. *Smith et al.* [2012] used a Rademacher distribution for the random factors of their $50,000$ clones (only values of $+1$ or -1 were allowed). Here, we use a Gaussian distribution, which enables the smaller number of clones to better represent the range of variability.

We perform the frozen eccentricity search at different inclinations with 25 clones of HgM005. The variability in frozen eccentricity reduces the suitable regions, in particular near $i = 0°$, $i = 65°$, and $i = 115°$ (see also Figure S6). Whereas the near-polar inclinations show more susceptibility to the HgM005 uncertainties than $i = 15 - 45°$ (and retrograde), they show that polar frozen orbits exist for eccentricities near 0.07, the value found with HgM005.

We performed propagations with GEODYN of polar orbits with eccentricities of 0.064, 0.068 and 0.074 (the spread over the 25 clones for $h = 500$ km and $i = 90°$). Each orbit configuration was integrated with HgM005 and with the two clone fields bounding the eccentricity values. Although the initial periapsis altitudes differ, of course, the orbit evolution is rather slow and appears sufficiently robust for future mission planning

consideration (Figure S6b). The long integration times (8.5 years) show that the initial larger variations are themselves periodic ($\sim$ 6 years) and would not lead to an impact. Near-circular polar frozen orbits are thus likely to exist at Mercury, a finding that would benefit the prospects for long-term exploration and monitoring of the inner planet and its dynamic environment. Of course, the orbit dynamics alone do not dictate the mission design, and the thermal environment in particular could be the most important constraint. We compared the planetary thermal radiation acceleration received along the orbit shown on Figure 11 with that received by MESSENGER during its first 100 days in orbit. Although the maximum flux is not significantly larger than for MESSENGER (Figure S7), the shorter orbital period ($\sim$ 2 h versus $\sim$ 12 h) sharply reduces the ability of the spacecraft to cool on the nightside. A more detailed study would be valuable but is outside the scope of this work.

The implications of the improved value of the $\bar{C}_{30}$ coefficient are especially important in the case of the BepiColombo Mercury Planetary Orbiter, as the initial orbit design anticipated the (then unknown) $\bar{C}_{30}$ to be positive. Its estimated value, $(-0.47659 \pm 0.0016) \times 10^{-5}$ (Table 3), thus leads to a decrease of the periapsis, and substantially more thermal forcing on the spacecraft components. This heating could be remedied by increasing the initial orbit altitude, and the better determination of $\bar{C}_{30}$ will facilitate the necessary modifications in mission planning.

7. Summary and Conclusions

We have analyzed three years of radio tracking data collected at Mercury by the MESSENGER spacecraft. We obtained a gravity field solution expanded to spherical harmonic degree and order 50, called HgM005, for which we also estimated the planetary orientation

and ephemeris of Mercury. We have described the geophysical implications of these new results, and we discussed in detail the modeling and error sources associated with the gravity anomalies and other important gravity parameters such as the low-degree zonal harmonics.

After successfully completing its one-year primary and one-year first extended missions, sufficient fuel reserves remained on MESSENGER to design a novel end-of-mission scenario. MESSENGERs second extended mission will take advantage of the decrease in periapsis altitude due to solar perturbations to execute four low-altitude campaigns, each spanning several weeks with periapsis altitudes lower than 100 km and as low as 25 km. During the first two of these periods, in September and October 2014, the periapsis will be in view of the Earth. With a periapsis latitude as low as $65°N$, the tracking of the spacecraft by the NASA DSN will give an exceptional view of the short-wavelength gravity anomalies over a large part of the northern hemisphere. For example, the majority of the western hemisphere between $50°N$ and $75°N$ will be mapped from altitudes less than 50 km. These data will yield a degree strength above 50 in the northern hemisphere, with the potential to substantially improve our understanding of the crustal structure of Mercury.

Acknowledgments. We thank the MESSENGER spacecraft and navigation teams for commanding and navigating the spacecraft during the interplanetary and orbital phases of the mission. The MESSENGER project is supported by the NASA Discovery Program under contracts NAS5-97271 to The Johns Hopkins University Applied Physics Laboratory and NASW-00002 to the Carnegie Institution of Washington. We thank David Rowlands for help with the GEODYN software, Mark Perry for his work with the NASA

DSN to acquire the radio tracking data that made this work possible, and Steven Hauck for input on the implications of the new field to interior structure. We also appreciate constructive comments on an earlier version of the manuscript by two reviewers. The data used in this paper and the HgM005 gravity field (the spherical harmonics coefficients, their associated uncertainties, and the full covariance matrix) are available at `http://geo.pds.nasa.gov/`. Localized correlations were computed using the SHTOOLS library (http://shtools.ipgp.fr). Several figures were created with the Generic Mapping Tools (GMT) software [*Wessel and Smith*, 1991].

References

Anderson, J. D., G. Colombo, P. B. Esposito, E. L. Lau, and G. B. Trager (1987), The mass, gravity field, and ephemeris of Mercury, *Icarus*, *71*, 337–349.

Antreasian, P. G., and G. W. Rosborough (1992), Prediction of radiant energy forces on the TOPEX/POSEIDON spacecraft, *J. Spacecraft and Rockets*, *29*, 81–90, doi:10.2514/3.26317.

Archinal, B. A., M. F. A'Hearn, E. Bowell, A. Conrad, G. J. Consolmagno, R. Courtin, T. Fukushima, D. Hestroffer, J. L. Hilton, G. A. Krasinsky, G. Neumann, J. Oberst, P. K. Seidelmann, P. Stooke, D. J. Tholen, P. C. Thomas, and I. P. Williams (2011), Report of the IAU Working Group on Cartographic Coordinates and Rotational Elements: 2009, *Celest. Mech. Dyn. Astron.*, *109*, 101–135, doi:10.1007/s10569-010-9320-4.

Brouwer, D., and G. M. Clemence (1961), *Methods of Celestial Mechanics*, Academic Press, New York, 598 pp.

Chin, G., S. Brylow, M. Foote, J. Garvin, J. Kasper, J. Keller, M. Litvak, I. Mitrofanov, D. Paige, K. Raney, M. Robinson, A. Sanin, D. Smith, H. Spence, P. Spudis, S. A. Stern, and M. Zuber (2007), Lunar Reconnaissance Orbiter overview: The instrument suite and mission, *Space Sci. Rev.*, *129*, 391–419, doi:10.1007/s11214-007-9153-y.

Cook, R. (1991), The long-term behavior of near-circular orbits in a zonal field, Spaceflight Mechanics Meeting, American Astronautical Society/American Institute of Aeronautics and Astronautics, AAS paper 91-453, February 13-11, Houston, Tex.

Davies, M. E., V. K. Abalakin, R. L. Duncombe, H. Masursky, B. Morando, T. C. Owen, P. K. Seidelmann, A. T. Sinclair, G. A. Wilkins, and C. A. Cross (1980), Report of the IAU working group on cartographic coordinates and rotational elements of the planets and satellites, *Celest. Mech.*, *22*, 205–230, doi:10.1007/BF01229508.

Delsate, N., P. Robutel, A. Lemaître, and T. Carletti (2010), Frozen orbits at high eccentricity and inclination: Application to Mercury orbiter, *Celest. Mech. Dyn. Astron.*, *108*, 275–300, doi:10.1007/s10569-010-9306-2.

Folkner, W. M. (2010), Planetary ephemeris DE423 fit to MESSENGER encounters with Mercury, *JPL Interoffice Memorandum*, *IOM 343R-10-001*, Jet Propulsion Laboratory, Pasadena, Calif.

Folkner, W. M., J. G. Williams, D. H. Boggs, R. S. Park, and P. Kuchynka (2014), The planetary and lunar ephemerides DE430 and DE431, *Interplanetary Network Progress Report*, *196*, 1–81.

Gambis, D. (2004), Monitoring Earth orientation using space-geodetic techniques: State-of-the-art and prospective, *J. Geodesy*, *78*, 295–303, doi:10.1007/s00190-004-0394-1.

Genova, A., L. Iess, and M. Marabucci (2013), Mercury's gravity field from the first six months of MESSENGER data, *Planet. Space Sci.*, *81*, 55–64, doi:10.1016/j.pss.2013.02.006.

Han, S.-C., E. Mazarico, and F. G. Lemoine (2009), Improved nearside gravity field of the Moon by localizing the power law constraint, *Geophys. Res. Lett.*, *36*, L11203, doi:10.1029/2009GL038556.

Hauck, S. A., II, J.-L. Margot, S. C. Solomon, R. J. Phillips, C. L. Johnson, F. G. Lemoine, E. Mazarico, T. J. McCoy, S. Padovan, S. J. Peale, M. E. Perry, D. E. Smith, and M. T. Zuber (2013), The curious case of Mercury's internal structure, *J. Geophys. Res. Planets*, *118*, 1204–1220, doi:10.1002/jgre.20091.

Head, J. W., C. R. Chapman, R. G. Strom, C. I. Fassett, B. W. Denevi, D. T. Blewett, C. M. Ernst, T. R. Watters, S. C. Solomon, S. L. Murchie, L. M. Prockter, N. L. Chabot, J. J. Gillis-Davis, J. L. Whitten, T. A. Goudge, D. M. H. Baker, D. M. Hurwitz, L. R. Ostrach, Z. Xiao, W. J. Merline, L. Kerber, J. L. Dickson, J. Oberst, P. K. Byrne, C. Klimczak, and L. R. Nittler (2011), Flood volcanism in the northern high latitudes of Mercury revealed by MESSENGER, *Science*, *333*, 1853–1856, doi:10.1126/science.1211997.

Iess, L., S. Asmar, and P. Tortora (2009), MORE: An advanced tracking experiment for the exploration of Mercury with the mission BepiColombo, *Acta Astronautica*, *65*, 666–675, doi:doi10.1016/j.actaastro.2009.01.049.

Kaula, W. M. (1966), *Theory of Satellite Geodesy. Applications of Satellites to Geodesy*, Blaisdell, Walham, Mass., 124 pp.

Klaasen, K. P. (1976), Mercury's rotation axis and period, *Icarus*, *28*, 469–478, doi: 10.1016/0019-1035(76)90120-2.

Konopliv, A. S., W. B. Banerdt, and W. L. Sjogren (1999), Venus gravity: 180th degree and order model, *Icarus*, *139*, 3–18.

Konopliv, A. S., S. W. Asmar, W. M. Folkner, O. Karatekin, D. C. Nunes, S. E. Smrekar, C. F. Yoder, and M. T. Zuber (2011), Mars high resolution gravity fields from MRO, Mars seasonal gravity, and other dynamical parameters, *Icarus*, *211*, 401–428, doi:10.1016/j.icarus.2010.10.004.

Konopliv, A. S., R. S. Park, D.-N. Yuan, S. W. Asmar, M. M. Watkins, J. G. Williams, E. Fahnestock, G. Kruizinga, M. Paik, D. Strekalov, N. Harvey, D. E. Smith, and M. T. Zuber (2013), The JPL lunar gravity field to spherical harmonic degree 660 from the GRAIL Primary Mission, *J. Geophys. Res. Planets*, *118*, 1415–1434, doi:10.1002/jgre.20097.

Konopliv, A. S., S. W. Asmar, R. S. Park, B. G. Bills, F. Centinello, A. B. Chamberlin, A. Ermakov, R. W. Gaskell, N. Rambaux, C. A. Raymond, C. T. Russell, D. E. Smith, P. Tricarico, and M. T. Zuber (2014), The Vesta gravity field, spin pole and rotation period, landmark positions, and ephemeris from the Dawn tracking and optical data, *Icarus*, *in press*, doi:10.1016/j.icarus.2013.09.005.

Lemoine, F. G. R., D. E. Smith, M. T. Zuber, G. A. Neumann, and D. D. Rowlands (1997), A 70th degree lunar gravity model (GLGM-2) from Clementine and other tracking data, *J. Geophys. Res.*, *102*, 16,339–16,359.

Lemoine, F. G., S. C. Kenyon, J. K. Factor, R. Trimmer, N. K. Pavlis, D. S. Chinn, C. M. Cox, S. M. Klosko, S. B. Luthcke, M. H. Torrence, Y. M. Wang, R. G. Williamson, E. C.

Pavlis, R. H. Rapp, and T. R. Olson (1998), The development of the joint NASA GSFC and NIMA geopotential model EGM96, NASA/TP-1998-206861: NASA Goddard Space Flight Center, Greenbelt.

Lemoine, F. G., D. E. Smith, D. D. Rowlands, M. T. Zuber, G. A. Neumann, D. S. Chinn, and D. E. Pavlis (2001), An improved solution of the gravity field of Mars (GMM-2B) from Mars Global Surveyor, *J. Geophys. Res.*, *106*, 23,359–23,376.

Lemoine, F. G., S. Goossens, T. J. Sabaka, J. B. Nicholas, E. Mazarico, D. D. Rowlands, B. D. Loomis, D. S. Chinn, D. S. Caprette, G. A. Neumann, D. E. Smith, and M. T. Zuber (2013), High-degree gravity models from GRAIL primary mission data, *J. Geophys. Res. Planets*, *118*, 1676–1698, doi:10.1002/jgre.20118.

Ma, X., and J. Li (2013), Artificial frozen orbits around Mercury, *Astrophys. Space Sci.*, *348*, 345–365, doi:10.1007/s10509-013-1575-2.

Margot, J.-L. (2009), A Mercury orientation model including non-zero obliquity and librations, *Celest. Mech. Dyn. Astron.*, *105*, 329–336, doi:10.1007/s10569-009-9234-1.

Margot, J. L., S. J. Peale, R. F. Jurgens, M. A. Slade, and I. V. Holin (2007), Large longitude libration of Mercury reveals a molten core, *Science*, *316*, 710–714, doi:10.1126/science.1140514.

Margot, J.-L., S. J. Peale, S. C. Solomon, S. A. Hauck, II, F. D. Ghigo, R. F. Jurgens, M. Yseboodt, J. D. Giorgini, S. Padovan, and D. B. Campbell (2012), Mercury's moment of inertia from spin and gravity data, *J. Geophys. Res.*, *117*, E00L09, doi:10.1029/2012JE004161.

Marshall, J. A., and S. B. Luthcke (1994), Radiative force model performance for TOPEX/Poseidon precision orbit determination, *J. Astronaut. Sci.*, *42*, 229–246.

Mazarico, E., M. T. Zuber, F. G. Lemoine, and D. E. Smith (2009), Effects of self-shadowing on nonconservative force modeling for Mars-orbiting spacecraft, *J. Spacecraft and Rockets*, *46*, 662–669, doi:10.2514/1.41679.

Mazarico, E., F. G. Lemoine, S.-C. Han, and D. E. Smith (2010), GLGM-3: A degree-150 lunar gravity model from the historical tracking data of NASA Moon orbiters, *J. Geophys. Res.*, *115*, E05001, doi:10.1029/2009JE003472.

Mazarico, E., D. D. Rowlands, G. A. Neumann, D. E. Smith, M. H. Torrence, F. G. Lemoine, and M. T. Zuber (2012), Orbit determination of the Lunar Reconnaissance Orbiter, *J. Geodesy*, *86*, 193–207, doi:10.1007/s00190-011-0509-4.

Mazarico, E. M., S. J. Goossens, F. G. Lemoine, D. E. Smith, M. T. Zuber, G. A. Neumann, M. H. Torrence, and S. C. Solomon (2013), The gravity field of Mercury derived from two years of MESSENGER data, in *Lunar Planet. Sci.*, 44, abstract 2429.

Montenbruck, O. and E. Gill (2000), Satellite Orbits, Springer, Heidelberg, 369 pp.

Moyer, T. D. (1981a), Transformation from proper time on Earth to coordinate time in solar system barycentric space-time of reference, 1, *Celest. Mech.*, *23*, 33–56, doi: 10.1007/BF01228543.

Moyer, T. D. (1981b), Transformation from proper time on Earth o coordinate time in solar system barycentric space-time of reference, 2, *Celest. Mech.*, *23*, p.57–68, doi: 10.1007/BF01228544.

Moyer, T. D. (2003), Formulation for Observed and Computed Values of Deep Space Network Observables, Wiley, Hoboken, N.J., 576 pp.

Padovan, S., J.-L. Margot, S. A. Hauck, II, W. B. Moore, and S. C. Solomon (2014), The tides of Mercury and possible implications for its interior structure, *J. Geophys. Res.*

Planets, *119*, 850–866, doi:10.1002/2013JE004459.

Paige, D. A., M. A. Siegler, J. K. Harmon, G. A. Neumann, E. M. Mazarico, D. E. Smith, M. T. Zuber, E. Harju, M. L. Delitsky, and S. C. Solomon (2013), Thermal stability of volatiles in the north polar region of Mercury, *Science*, *339*, 300–303, doi: 10.1126/science.1231106.

Pavlis, D. E., J. Wimert, and J. J. McCarthy (2013), GEODYN II system description, vols. 1-5, *contractor report*, SGT Inc., Greenbelt, Md.

Peale, S. J., R. J. Phillips, S. C. Solomon, D. E. Smith, and M. T. Zuber (2002), A procedure for determining the nature of Mercury's core, *Meteorit. Planet. Sci.*, *37*, 1269–1283, doi:10.1111/j.1945-5100.2002.tb00895.x.

Perry, M. E., D. S. Kahan, O. S. Barnouin, C. M. Ernst, S. C. Solomon, M. T. Zuber, D. E. Smith, R. J. Phillips, S. A. Hauck, II, G. A. Neumann, S. J. Peale, J. L. Margot, E. Mazarico, C. L. Johnson, R. W. Gaskell, J. H. Roberts, S. W. Asmar, and R. L. McNutt. (2013), Radio frequency occultations show that Mercury is oblate, in *Lunar Planet. Sci.*, 44, abstract 2485.

Pettengill, G. H., and R. B. Dyce (1965), A radar determination of the rotation of the planet Mercury, *Nature*, *206*, 1240, doi:10.1038/2061240a0.

Ray, R. D. (2013), Precise comparisons of bottom-pressure and altimetric ocean tides, *J. Geophys. Res. Oceans*, *118*, 4570–4584, doi:10.1002/jgrc.20336.

Rivoldini, A., T. Van Hoolst, and O. Verhoeven (2009), The interior structure of Mercury and its core sulfur content, *Icarus*, *201*, 12–30, doi:10.1016/j.icarus.2008.12.020.

Rivoldini, A., and T. Van Hoolst (2013), The interior structure of Mercury constrained by the low-degree gravity field and the rotation of Mercury, *Earth Planet. Sci. Lett.*,

377–378, 62–72, doi:10.1016/j.epsl.2013.07.021.

Shapiro, I.I. (1989), Observed value of the advance of the perihelion of Mercury, in *General Relativity and Gravitation*, edited by N.Ashby, D.F. Bartlett, and W.Wyss, pp.313–330, Cambridge Univ. Press, New York.

Smith, D.E. (2014), GTMES_120V02_SHA, MESS-H-RSS_MLA-5-SDP-V1, *NASA Planetary Data System*, `http://geo.pds.nasa.gov/messenger/mess-h-rss_mla-5-sdp-v1/messrs_1001/data/shadr/`.

Smith, D. E., M. T. Zuber, R. J. Phillips, S. C. Solomon, G. A. Neumann, F. G. Lemoine, S. J. Peale, J.-L. Margot, M. H. Torrence, M. J. Talpe, J. W. Head III, S. A. Hauck, II, C. L. Johnson, M. E. Perry, O. S. Barnouin, R. L. McNutt Jr., and J. Oberst (2010), The equatorial shape and gravity field of Mercury from MESSENGER flybys 1 and 2, *Icarus*, *209*, 88–100, doi:10.1016/j.icarus.2010.04.007.

Smith, D. E., M. T. Zuber, R. J. Phillips, S. C. Solomon, S. A. Hauck, II, F. G. Lemoine, E. Mazarico, G. A. Neumann, S. J. Peale, J.-L. Margot, C. L. Johnson, M. H. Torrence, M. E. Perry, D. D. Rowlands, S. Goossens, J. W. Head III, and A. H. Taylor (2012), Gravity field and internal structure of Mercury from MESSENGER, *Science*, *336*, 214–217, doi:10.1126/science.1218809.

Spada, G. (2008), ALMA, a Fortran program for computing the viscoelastic Love numbers of a spherically symmetric planet, *Computers Geosci.*, *34*, p.667–687, doi:10.1016/j.cageo.2007.12.001.

Srinivasan, D. K., M. E. Perry, K. B. Fielhauer, D. E. Smith, and M. T. Zuber (2007), The radio frequency subsystem and radio science on the MESSENGER mission, *Space Sci. Rev.*, *131*, 557–571, doi:10.1007/s11214-007-9270-7.

Tapley, B. D., B. E. Schutz, and G. H. Born (2004), *Statistical Orbit Determination*, Elsevier, Burlington, Mass., 547 pp.

Van Hoolst, T. and G. Jacobs (2003), Mercury's tides and interior structure, *J. Geophys. Res.*, *108*, 5121, doi:10.1029/2003JE002126.

Van Hoolst, T., F. Sohl, I. Holin, O. Verhoeven, V. Dehant, and T. Spohn (2007), Mercury's interior structure, rotation, and tides, *Space Sci. Rev.*, *132*, 203–227, doi:10.1007/s11214-007-9202-6.

Verma, A. K., A. Fienga, J. Laskar, H. Manche, and M. Gastineau (2014), Use of MESSENGER radioscience data to improve planetary ephemeris and to test general relativity, *Astron. Astrophys.*, *561*, A115, doi:10.1051/0004-6361/201322124.

Wessel, P. and W.H.F. Smith (1991), Free software helps map and display data, *Eos Trans. AGU*, *72*, 441, 445–446.

Wieczorek, M. A., and R. J. Phillips (1998), Potential anomalies on a sphere: Applications to the thickness of the lunar crust, *J. Geophys. Res.*, *103*, 1715–1724, doi:10.1029/97JE03136.

Wieczorek, M. A., and F. J. Simons (2005), Localized spectral analysis on the sphere, *Geophys. J. Int.*, *162*, 655–675, doi:10.1111/j.1365-246X.2005.02687.x.

Zuber, M. T., D. E. Smith, R. J. Phillips, S. C. Solomon, G. A. Neumann, S. A. Hauck, II, S. J. Peale, O. S. Barnouin, J. W. Head III, C. L. Johnson, F. G. Lemoine, E. Mazarico, X. Sun, M. H. Torrence, A. M. Freed, C. Klimczak, J.-L. Margot, J. Oberst, M. E. Perry, R. L. McNutt Jr., J. A. Balcerski, N. Michel, M. J. Talpe, and D. Yang (2012), Topography of the northern hemisphere of Mercury from MESSENGER laser altimetry, *Science*, *336*, 217–220, doi:10.1126/science.1218805.

Zuber, M. T., D. E. Smith, M. M. Watkins, S. W. Asmar, A. S. Konopliv, F. G. Lemoine, H. J. Melosh, G. A. Neumann, R. J. Phillips, S. C. Solomon, M. A. Wieczorek, J. G. Williams, S. J. Goossens, G. Kruizinga, E. Mazarico, R. S. Park, and D.-N. Yuan (2013), Gravity field of the Moon from the Gravity Recovery and Interior Laboratory (GRAIL) mission, *Science*, *339*, 668–671, doi:10.1126/science.1231507.

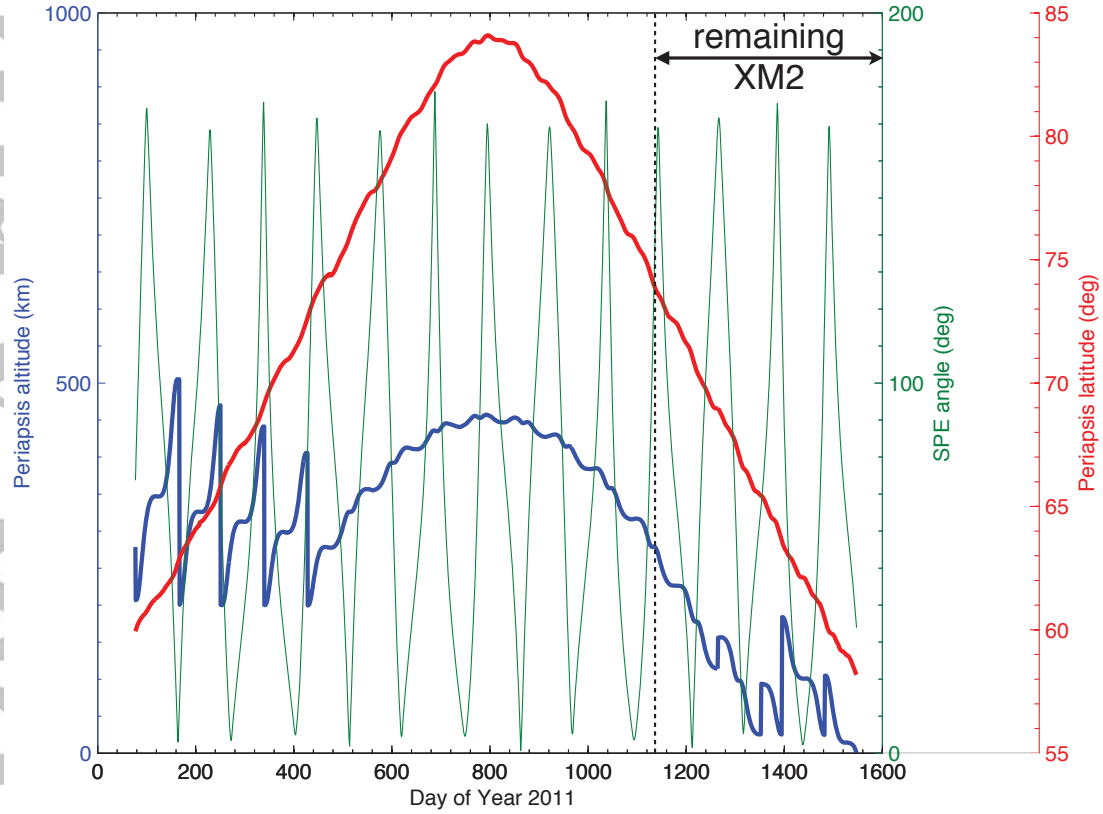

Figure 1. MESSENGER periapsis altitude (blue), periapsis latitude (red), and Sun-probe-Earth (SPE) angle (green) during the orbital mission phase, including predictions for the remainder of the second extended mission (XM2).

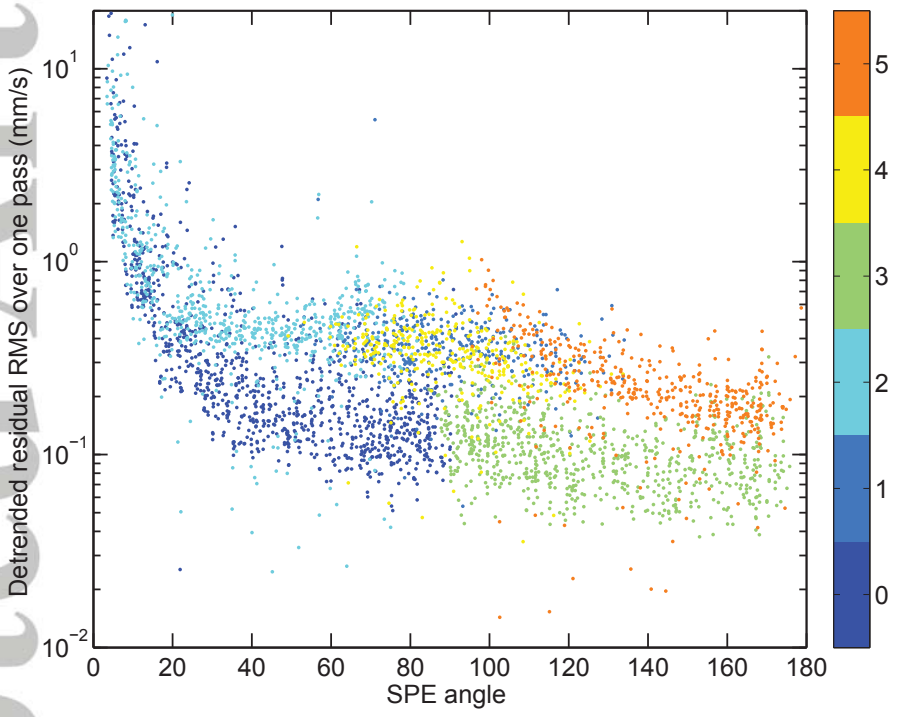

Figure 2. Noise level of the individual tracking passes of MESSENGER, measured as the root mean square of the Doppler residuals over short and detrended segments and plotted against the Sun-probe-Earth angle. Each integer on the color bar indicates a separate MESSENGER antenna, following the PDS Frames Kernel for the radio science experiment. Antennas 0 and 3 are HGA/MGAs, whereas the rest are LGAs.

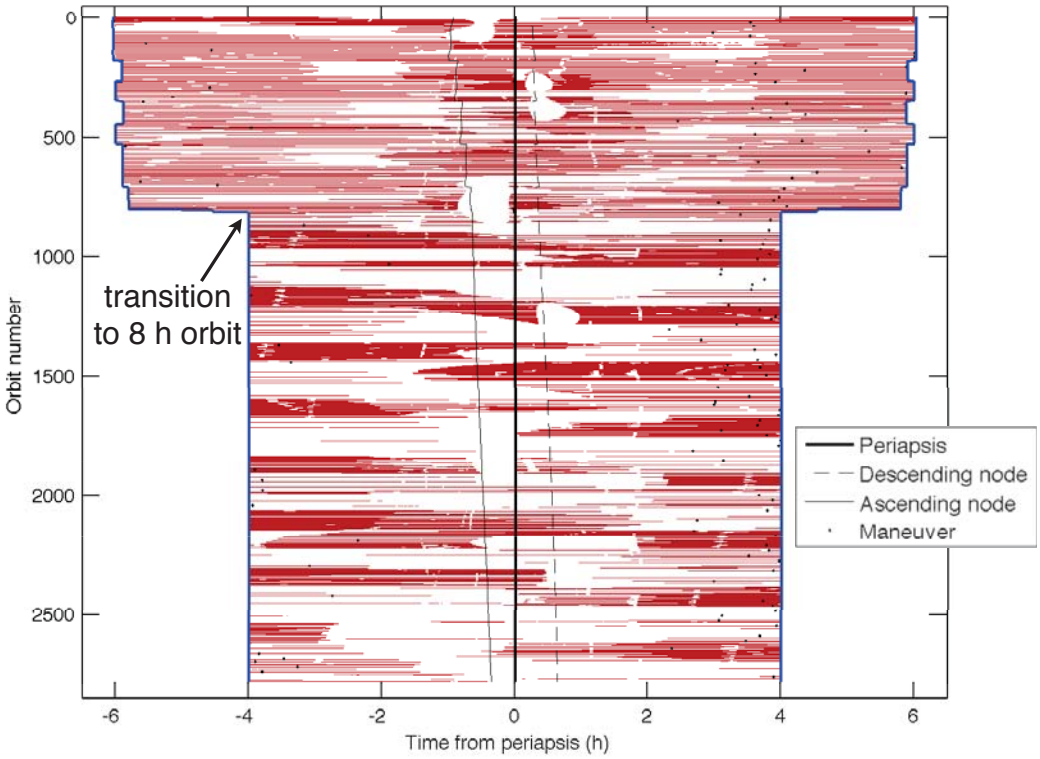

Figure 3. Summary of tracking data coverage of the MESSENGER spacecraft during the orbital mission phase. Each line represents one orbit, and DSN passes are shown in red. Black dots indicate a spacecraft maneuver.

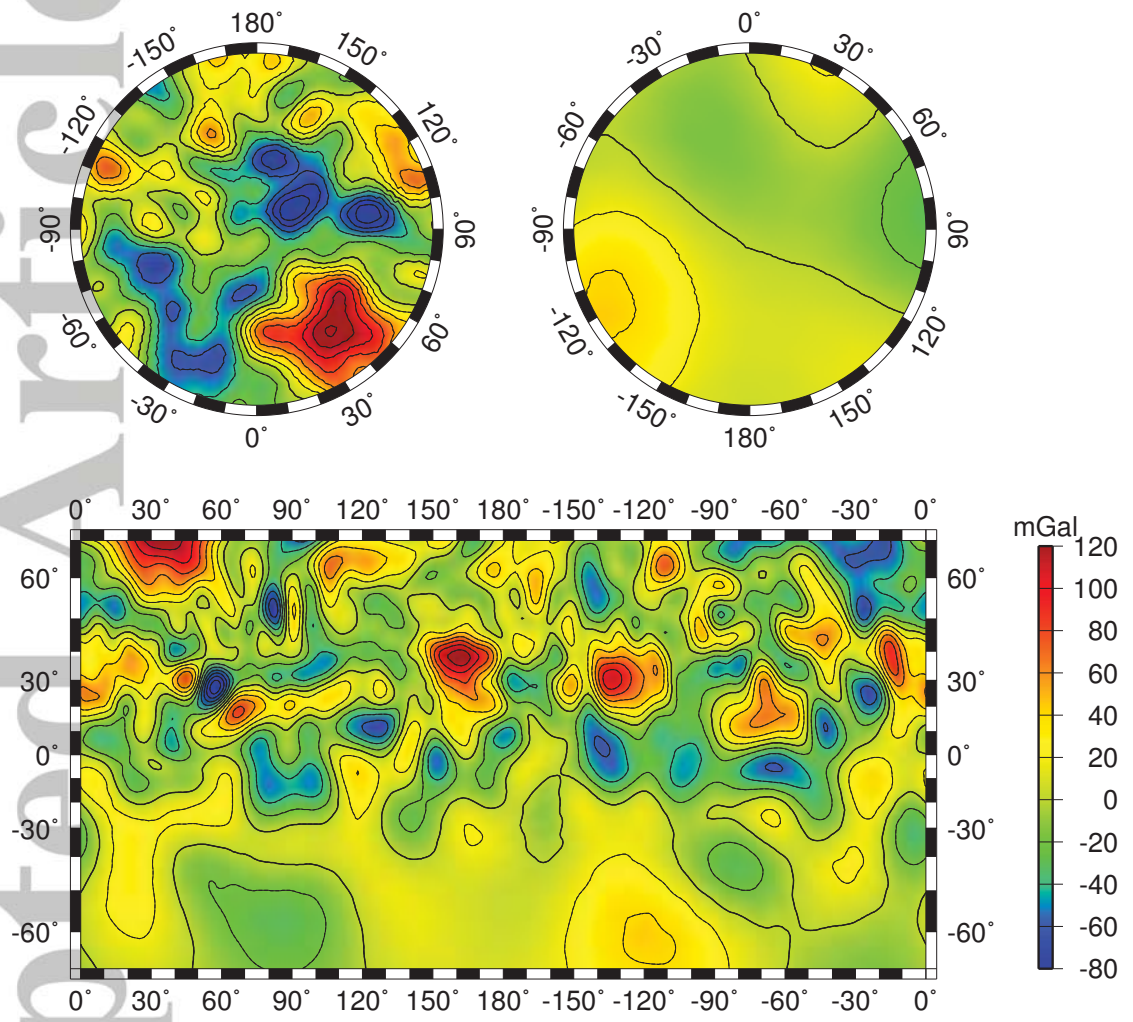

Figure 4. The gravity anomaly field (in mGal) of solution HgM005, to harmonic degree and order 50. Mercator projection to 67° latitude (bottom) and polar stereographic projections over the north (top left) and south (top right) poles down to 60° latitude. Contour interval is 20 mGal.

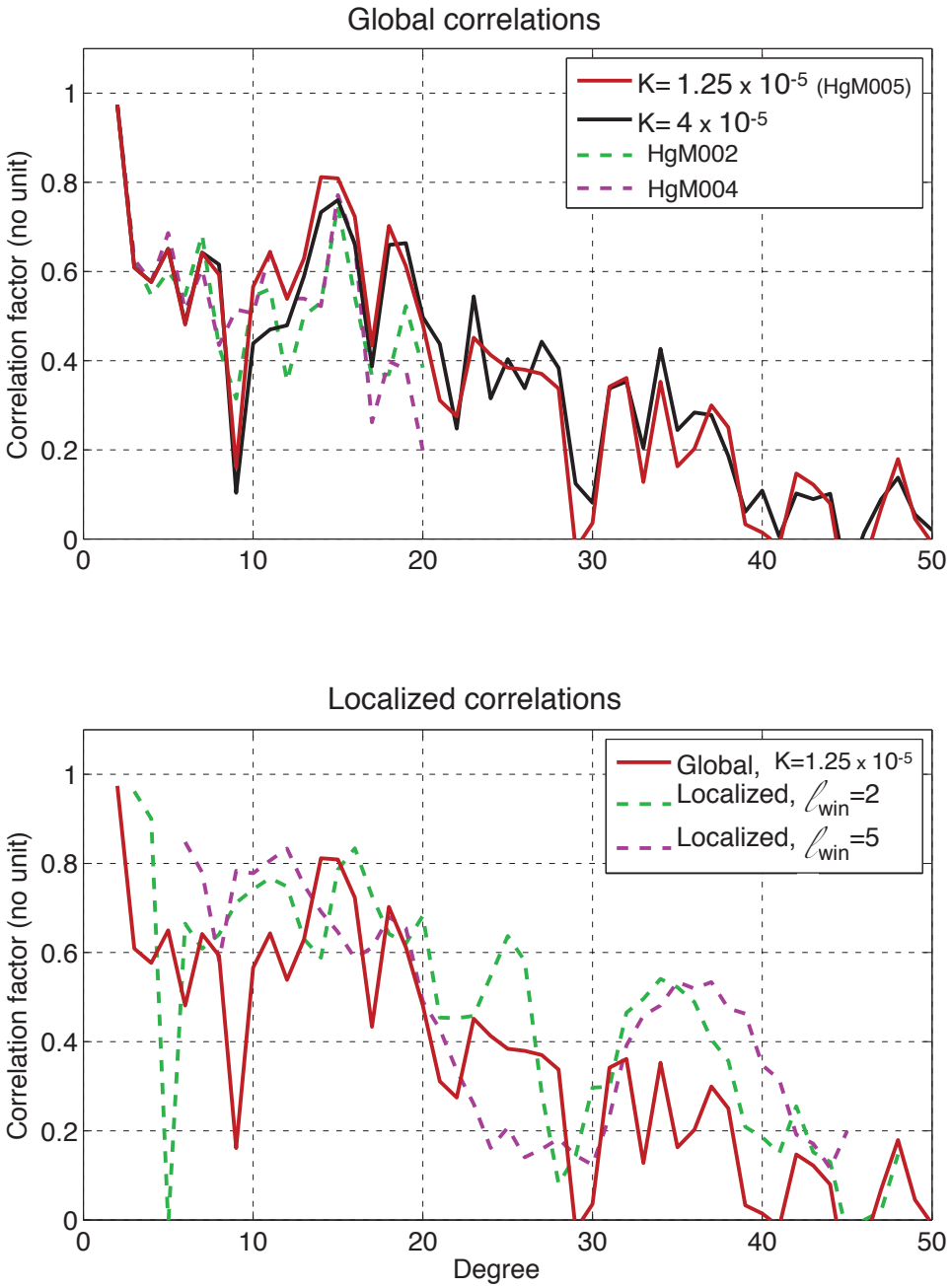

Figure 5. Correlation of MESSENGER-derived gravity models with the global shape model determined from MLA and radio occultation measurements. We show the global correlations (top) and the correlations of the fields after localization around the north pole with different windowing tapers (bottom). K is the Kaula factor, with a smaller number indicating a stronger constraint on the field power (see Section 4.1).

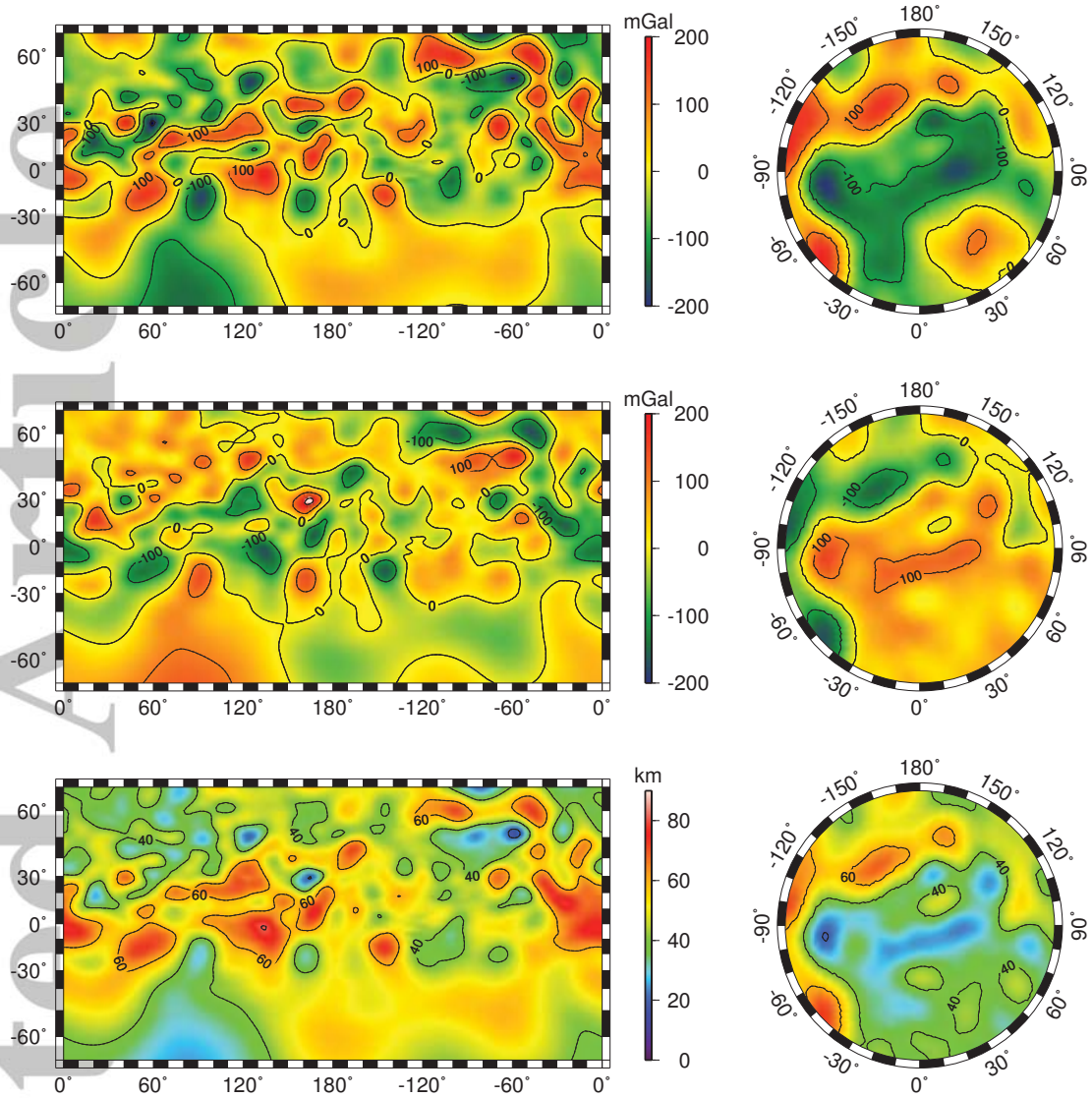

Figure 6. (top) Gravity anomaly field (in mGal) predicted by surface topographic relief, inferred from MLA measurements and radio occultations, for a crustal density of $\rho = 3200 kgm^{-3}$. At left is a Mercator projection to 67° latitude, and at right a north polar stereographic projection for latitudes 60–90°N. (middle) Bouguer gravity anomaly field (in mGal), obtained by subtracting the top gravity field from the free-air gravity anomaly field in Figure 4. (bottom) Crustal thickness (in km), obtained from first-order downward continuation of the Bouguer gravity anomaly. At each location, the spherical harmonic representation is expanded only up to the spatial degree strength of HgM005 (Figure 8).

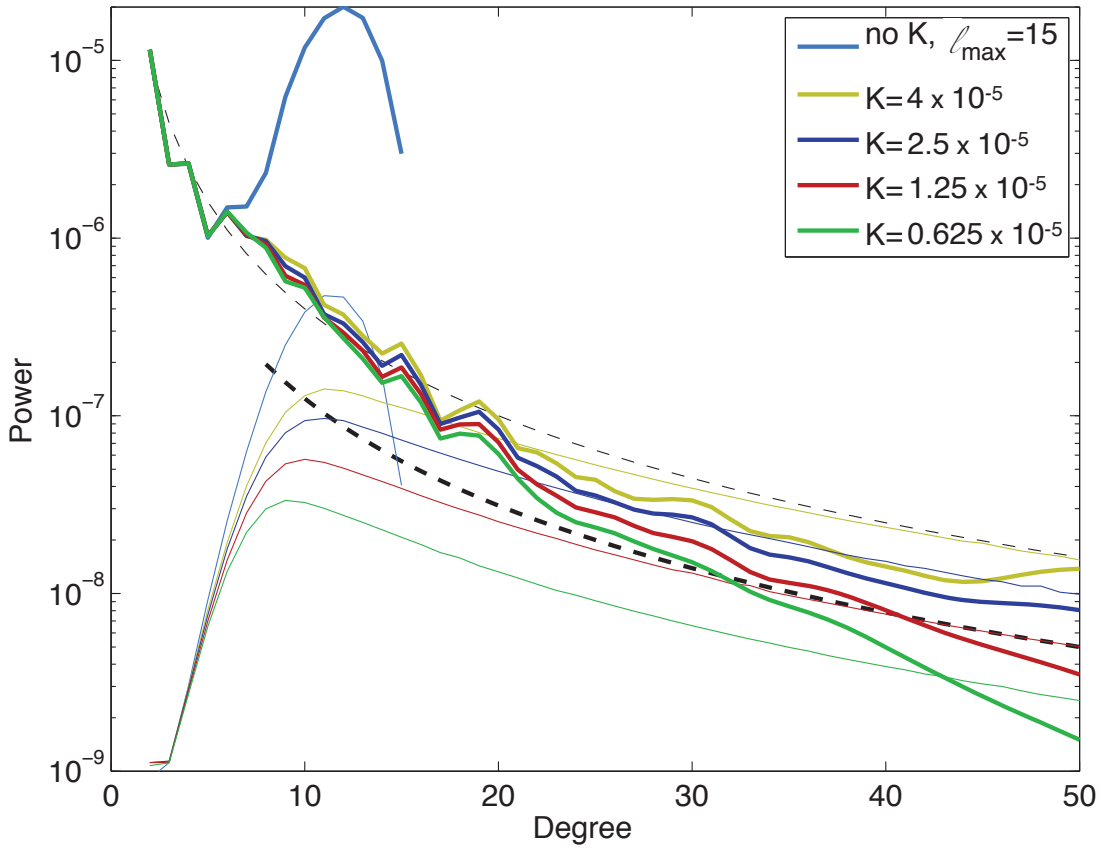

Figure 7. RMS power of gravity solutions obtained with different Kaula factors (thick colored lines) and associated formal error spectra (thin colored lines). Our preferred solution, HgM005, is shown in red. The *a priori* Kaula factor ($K = 4 \times 10^{-5}$) is shown by a thin dashed line. The preferred Kaula factor ($K = 1.25 \times 10^{-5}$), shown as a thick dashed black line, was applied for $l > 7$.

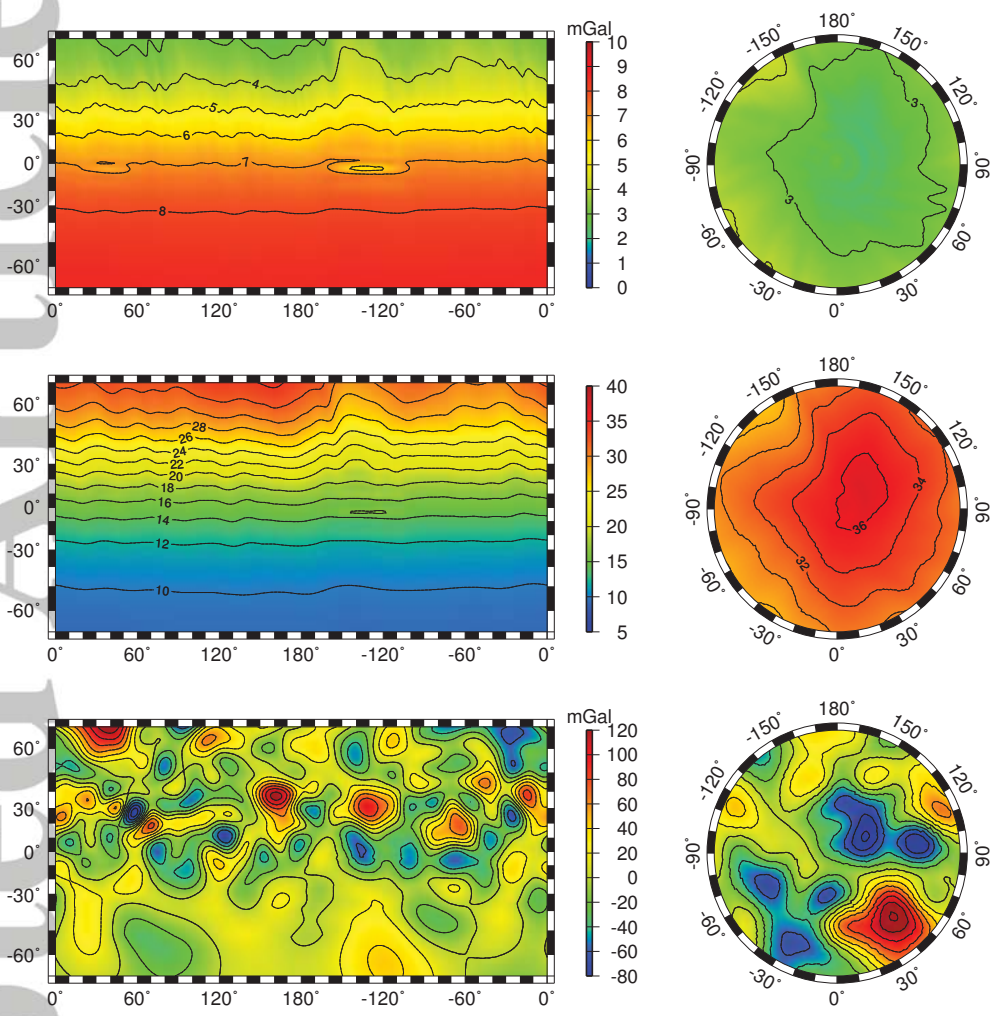

Figure 8. (top) Gravity anomaly errors (in mGal) obtained from the HgM005 covariance. (middle) HgM005 degree strength computed from the comparison of the Kaula regularization and the full covariance matrix. Features smaller than the degree-strength-equivalent wavelength are not robust. (bottom) Free-air gravity anomaly field (in mGal) of HgM005, expanded at every location only up to the local degree strength. Same projections as in Figure 6.

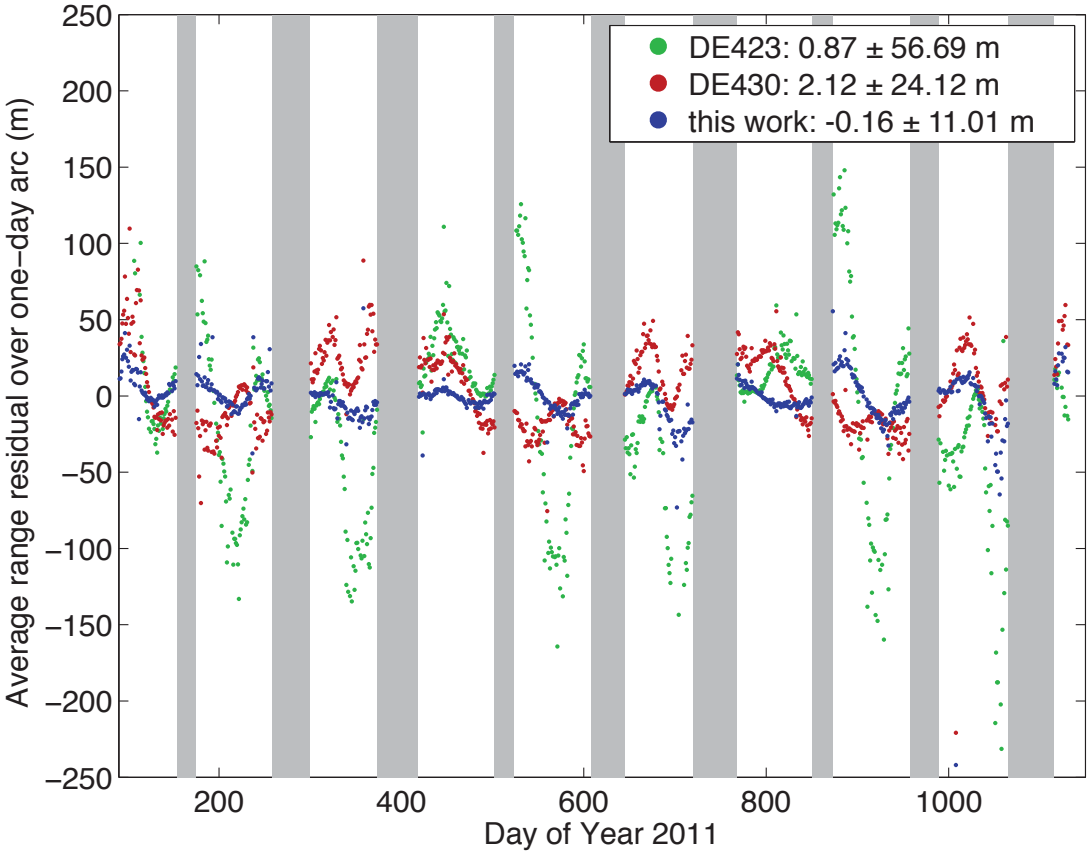

Figure 9. Range residuals during MESSENGER's orbital mission phase, obtained after arc convergence with the DE423 ephemeris (green), the DE430 ephemeris (red), and our adjustment (blue). Each point represents the average range residual over a one-day arc. Data affected by high plasma noise (intervals when SPE $< 40°$, indicated in gray) are not shown for clarity. The median and standard deviation of each time series are indicated in the legend.

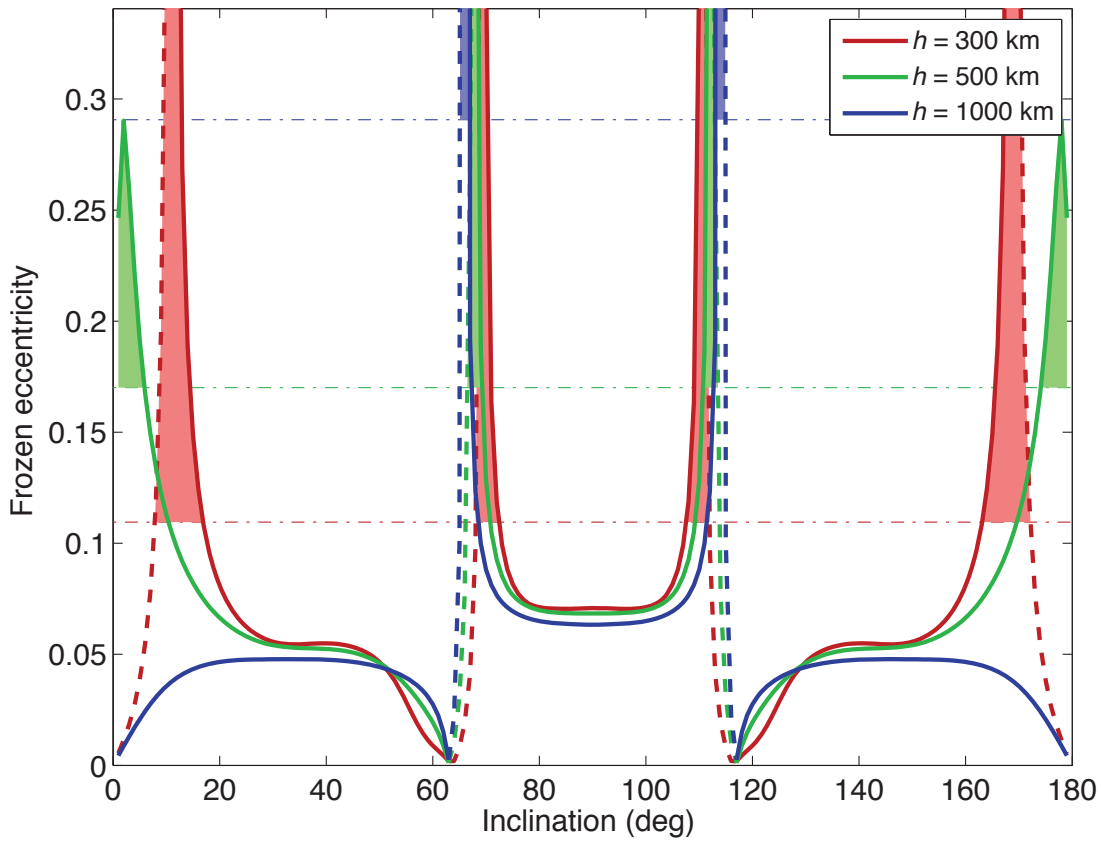

Figure 10. Computed eccentricity for frozen orbits of varied inclination and semi-major axis (referenced to $R = 2440$ km to yield altitude h). Filled areas indicate that the frozen eccentricity is above the maximum acceptable eccentricity (dot-dashed line) and would lead to surface impact. Dashed lines indicate that the argument of pericenter ω is 90°, whereas solid lines indicate $\omega = 270°$ (pericenter over the southern hemisphere). Only the zonal gravity coefficients of HgM005 were considered.

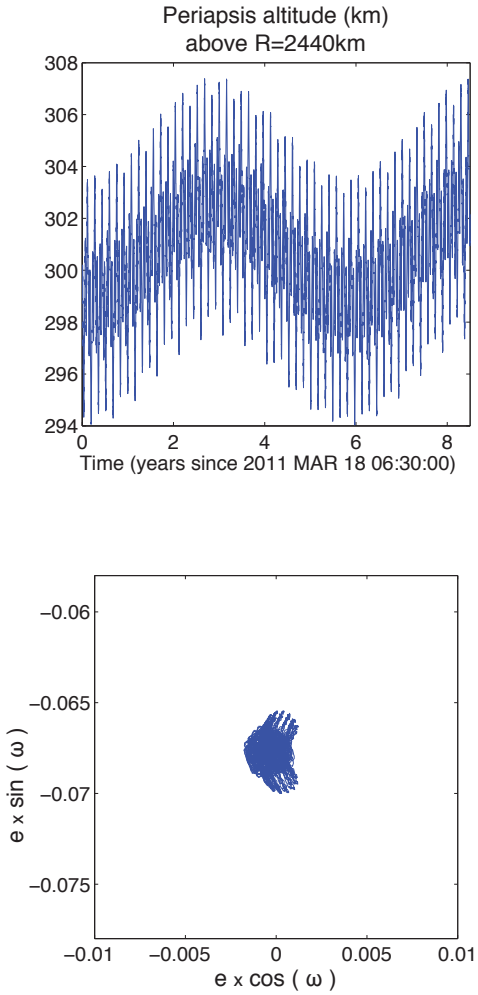

Figure 11. Orbit evolution for the $h = 500$ km, $i = 90°$ frozen orbit (found in Figure 10), as propagated over 8.5 years with the full HgM005 field and additional perturbations. (top) Periapsis altitude (in km). (bottom) Equinoctial element plot, showing the stability of the orbital elements.

Table 1. Model parameters used with ALMA [*Spada*, 2008], and the resulting tidal Love number k_2.

Elastic thickness	Mantle rigidity	FeS layer rigidity	Computed k_2
70 km	75 GPa	-	0.46
90 km	75 GPa	-	0.46
70 km	65 GPa	35 GPa	0.55
70 km	95 GPa	35 GPa	0.52
70 km	10 GPa	35 GPa	0.62

Table 2. Kaula factor for Mercury inferred by scaling [*Konopliv et al.*, 2014] from other planetary bodies.

Planetary body	Kaula factor	Mass[a] (kg)	Radius[b] (km)	Scaled Kaula	Reference
Earth	7.07×10^{-6}	5.97×10^{24}	6378.0	4.96×10^{-5}	*Lemoine et al.* [1998]
Moon	3.6×10^{-4}	7.35×10^{22}	1738.0	6.94×10^{-5}	*Lemoine et al.* [2013]
Venus	1.2×10^{-5}	4.87×10^{24}	6051.0	6.91×10^{-5}	*Konopliv et al.* [1999]
Mars	18.4×10^{-5}	6.42×10^{23}	3396.0	1.86×10^{-4}	*Lemoine et al.* [2001]
Vesta	1.1×10^{-2}	2.59×10^{20}	265.0	4.87×10^{-5}	*Konopliv et al.* [2014]

[a] From the JPL DE423 ephemeris [*Folkner*, 2010].

[b] Reference radius for the gravity fields. Typically the same as the IAU convention, except for the Moon and Vesta.

Table 3. Estimated values and formal uncertainties of selected low-degree coefficients

Coefficient	Value	Formal uncertainty (σ)	Ratio (C_{lm}/σ)
$\bar{C}_{20}$	-2.25045×10^{-5}	6.8×10^{-10}	-
$\bar{C}_{22}$	1.24538×10^{-5}	4.4×10^{-10}	-
$\bar{C}_{30}$	-0.47659×10^{-5}	1.6×10^{-8}	-
$\bar{C}_{21}$	-1.61527×10^{-8}	3.8×10^{-10}	~ 42
$\bar{S}_{21}$	-1.36488×10^{-8}	3.9×10^{-10}	~ 35
$\bar{S}_{22}$	-2.09078×10^{-8}	2.3×10^{-9}	~ 9

Table 4. Brouwer-Clemence SET III parameter corrections, and associated ephemeris Keplerian element corrections.

Parameter	Unit	Value	Parameter	Unit	Value
$\Delta a/a$	-	4.48×10^{-12}	Δa	m	0.26
Δe	-	-8.83×10^{-10}	Δe	-	-8.83×10^{-10}
$\Delta M_0 + \Delta\omega$	$^\circ$	2.52×10^{-10}	Δi	$^\circ$	-1.40×10^{-6}
Δp	$^\circ$	-5.27×10^{-10}	$\Delta\Omega$	$^\circ$	2.30×10^{-6}
Δq	$^\circ$	2.48×10^{-8}	$\Delta\omega$	$^\circ$	-2.25×10^{-6}
$e\Delta\omega$	$^\circ$	1.15×10^{-10}	ΔM	$^\circ$	-